

AD-A034 384

ARNOLD ENGINEERING DEVELOPMENT CENTER ARNOLD AIR FORCE--ETC F/G 14/2
THE DEVELOPMENT OF A DISPLACEMENT INTERFEROMETER FOR MODEL DEFL--ETC(U)
JAN 77 B W BOMAR, W H GOETHERT, R A BELZ

UNCLASSIFIED

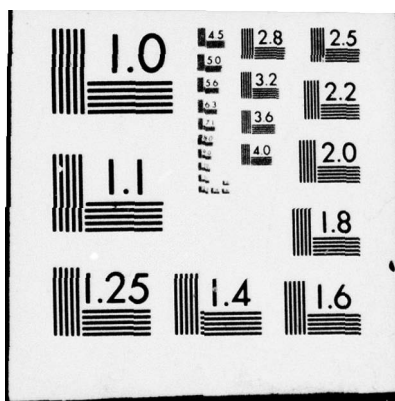
AEDC-TR-76-116

NL

1 OF 1
AD-A
034 384



END
DATE
FILMED
2-15-77
NTIS



U.S. DEPARTMENT OF COMMERCE
National Technical Information Service

AD-A034 384

THE DEVELOPMENT OF A DISPLACEMENT INTERFEROMETER
FOR MODEL DEFLECTION MEASUREMENTS

ARNOLD ENGINEERING DEVELOPMENT CENTER
ARNOLD AIR FORCE STATION, TENNESSEE

JANUARY 1977

ADA034384

018052

AEDC-TR-76-116



**THE DEVELOPMENT OF A DISPLACEMENT
INTERFEROMETER FOR MODEL
DEFLECTION MEASUREMENTS**

**OFFICE OF THE TECHNICAL DIRECTOR
ARNOLD ENGINEERING DEVELOPMENT CENTER
AIR FORCE SYSTEMS COMMAND
ARNOLD AIR FORCE STATION, TENNESSEE 37389**

January 1977

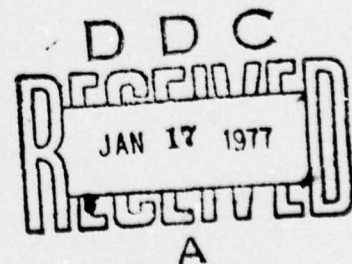
Final Report for Period July 1974 — June 1976

Approved for public release; distribution unlimited.

REPRODUCED BY
NATIONAL TECHNICAL
INFORMATION SERVICE
U. S. DEPARTMENT OF COMMERCE
SPRINGFIELD, VA. 22161

Prepared for

**DIRECTORATE OF TECHNOLOGY (DY)
ARNOLD ENGINEERING DEVELOPMENT CENTER
ARNOLD AIR FORCE STATION, TENNESSEE 37389**



NOTICES

When U. S. Government drawings specifications, or other data are used for any purpose other than a definitely related Government procurement operation, the Government thereby incurs no responsibility nor any obligation whatsoever, and the fact that the Government may have formulated, furnished, or in any way supplied the said drawings, specifications, or other data, is not to be regarded by implication or otherwise, or in any manner licensing the holder or any other person or corporation, or conveying any rights or permission to manufacture, use, or sell any patented invention that may in any way be related thereto.

Qualified users may obtain copies of this report from the Defense Documentation Center

References to named commercial products in this report are not to be considered in any sense as an endorsement of the product by the United States Air Force or the Government.

This report has been reviewed by the Information Office (OI) and is releasable to the National Technical Information Service (NTIS). At NTIS, it will be available to the general public, including foreign nations.

APPROVAL STATEMENT

This technical report has been reviewed and is approved for publication.

FOR THE COMMANDER

Marshall K Kingery

MARSHALL K. KINGERY
Research & Development
Division
Directorate of Technology

Robert O Dietz

ROBERT O. DIETZ
Director of Technology

UNCLASSIFIED

REPORT DOCUMENTATION PAGE		READ INSTRUCTIONS BEFORE COMPLETING FORM
1. REPORT NUMBER AEDC-TR-76-116	2. GOVT ACCESSION NO.	3. RECIPIENT'S CATALOG NUMBER
4. TITLE (and Subtitle) THE DEVELOPMENT OF A DISPLACEMENT INTERFEROMETER FOR MODEL DEFLECTION MEASUREMENTS	5. TYPE OF REPORT & PERIOD COVERED Final Report - July 1974 June 1976	
	6. PERFORMING ORG. REPORT NUMBER	
7. AUTHOR(s) B. W. Bomar, W. H. Goethert, R. A. Belz, and H. T. Bentley, III, ARO, Inc.	8. CONTRACT OR GRANT NUMBER(s)	
9. PERFORMING ORGANIZATION NAME AND ADDRESS Arnold Engineering Development Center (DY) Air Force Systems Command Arnold Air Force Station, Tennessee 37389	10. PROGRAM ELEMENT, PROJECT, TASK AREA & WORK UNIT NUMBERS Program Element 65807F	
11. CONTROLLING OFFICE NAME AND ADDRESS Arnold Engineering Development Center (DYFS) Arnold Air Force Station, Tennessee 37389	12. REPORT DATE January 1977	
	13. NUMBER OF PAGES 58	
14. MONITORING AGENCY NAME & ADDRESS (if different from Controlling Office)	15. SECURITY CLASS. (of this report) UNCLASSIFIED	
	15a. DECLASSIFICATION/DOWNGRADING SCHEDULE N/A	
16. DISTRIBUTION STATEMENT (of this Report) Approved for public release; distribution unlimited.		
17. DISTRIBUTION STATEMENT (of the abstract entered in Block 20, if different from Report)		
18. SUPPLEMENTARY NOTES Available in DDC		
19. KEY WORDS (Continue on reverse side if necessary and identify by block number) <div style="display: flex; justify-content: space-between;"> <div> interferometers lasers displacement (differential) steady state </div> <div> time variant deflection measurement wavelengths </div> </div>		
20. ABSTRACT (Continue on reverse side if necessary and identify by block number) <p>A two-beam laser interferometric device capable of continuously measuring either absolute or differential displacement (both steady state and time variant) with a resolution to one-quarter of the laser wavelength is described. This device is proposed for measurement of model attitude and deflection in wind tunnel applications. Experiments are presented demonstrating its accuracy, versatility, and online readout capabilities. A</p>		

UNCLASSIFIED

UNCLASSIFIED

20. ABSTRACT (Continued)

conceptual multibeam device to extend the present device for simultaneous measurement of pitch, roll, twist, and deflection is also discussed.

APSC
Arnold AFS Tenn

UNCLASSIFIED 

PREFACE

The work reported herein was conducted by the Arnold Engineering Development Center (AEDC), Air Force Systems Command (AFSC), under Program Element 65807F. The results of the research presented were obtained by ARO, Inc. (a subsidiary of The Sverdrup Corporation), contract operator of AEDC, AFSC, Arnold Air Force Station, Tennessee. The work was conducted under ARO Project Nos. V37A-30A and B32A-06A. The authors of this report were B. W. Bomar, W. H. Goethert, R. A. Belz, and H. T. Bentley, III, ARO, Inc. The manuscript (ARO Control No. ARO-OMD-TR-76-79) was submitted for publication on July 22, 1976.

ACCESSION for	
ETIS	Write Section <input checked="" type="checkbox"/>
DOC	Buff Section <input type="checkbox"/>
UNANNOUNCED	<input type="checkbox"/>
JUSTIFICATION	
BY	
DISTRIBUTION/AVAILABILITY CODES	
Dist.	AVAIL. CODE OR SPECIAL
A	

CONTENTS

	<u>Page</u>
1.0 INTRODUCTION	7
2.0 OPTICAL SYSTEM ANALYSIS	
2.1 Two-Beam Optical System	8
2.2 Proposed Multiple-Beam System	11
2.3 Optical Signal-Mixing Requirements	14
2.4 Retroreflector Analysis	15
2.5 Angular Motion Limitations	17
2.6 Laser Power and Photodetector Sensitivity	20
3.0 DISPLACEMENT INTERFEROMETER SIGNAL PROCESSORS	
3.1 Phase Quadrature Digital Data Processor	23
3.2 Analog Data Processor	29
3.3 Evaluation of Digital and Analog Processors	34
4.0 DISPLACEMENT ERROR ANALYSIS	
4.1 Laser Frequency and Optical System Stability	44
4.2 Density Effects	45
5.0 SUMMARY AND CONCLUSIONS	50
REFERENCES	51

ILLUSTRATIONS

Figure

1. Two-Beam Optical System Schematic	9
2. Conceptual Multiple-Beam Optical System	12
3. Beam-Combining Optical Blocks	13
4. Variation of the Effective Aperture of a Circular Retroreflector with Angle of Incidence	16
5. Retroreflector Motion within a Collimated Illumination Beam	
a. Nominal Illumination ($\theta_i = 0$)	18
b. Rotation with the Angle of Incidence	18

<u>Figure</u>	<u>Page</u>
c. Rotation Opposite to the Angle of Incidence	18
d. Rotation through the Illuminating Beams	18
6. Retroreflector Motion within a Finite Diameter, Collimated, Illumination Beam	19
7. Phase Quadrature Position Data Processor	25
8. Analog Waveforms and Logic Pulse Trains for the Phase Quadrature Signal Processor	26
9. Pictorial Representation of Surface Motion-Generating Phase-Delayed Signals P_1 and P_2	27
10. Logic Waveforms of Surface Motion Depicted in Fig. 9	28
11. Circuit Waveforms from the $\lambda/4$ Resolution Digital Processor	
a. Circuit Waveforms at Surface Turnaround	30
b. Circuit Generation of the $A \cdot \bar{B} \cdot C_\delta$ Term from Eq. (27)	30
c. Transfer of Position Pulses at Surface Turnaround	30
12. Analog Readout, Frequency-to-Voltage Converter	31
13. Experimental Setup for the Vibrating Bar Experiment	35
14. Flow Chart for Data Processing of Vibrating Bar Experiment	36
15. Data from Run No. 1	
a. Online Velocity Data from Analog Readout	38
b. Integrated Velocity of Fig. 15a	39
c. Online Displacement Data from Digital Readout	39
16. Data from Run No. 2	
a. Online Velocity Data from Analog Readout	40

<u>Figure</u>	<u>Page</u>
b. Integrated Velocity of Fig. 16a	41
c. Online Displacement from Digital Readout	41
d. Instant Recall of Last 25 percent of Fig. 16c	42
17. Data from Run No. 3	
a. Online Velocity Data from Analog Readout	43
b. Integrated Velocity of Fig. 17a	43
c. Online Displacement from Digital Readout	44
18. Total-Pressure Operating Envelopes for PWT Tunnels 16T and 16S	46

TABLES

1. Multiple-Beam Optical System Parameters and Required Laser Power	22
2. Tunnels 16T/S Conditions	48
NOMENCLATURE	53

1.0 INTRODUCTION

Model displacement and the relative position of the wings with respect to the fuselage are important measurements in aerodynamic testing programs. The amount of actual model pitch, roll, and yaw, in addition to magnitude and frequency of wing and fuselage oscillations, are all pertinent to the aerodynamic measurements of a test model (Ref. 1). These are especially critical in high Reynolds number test conditions where aerodynamic loading can be sufficient to produce large static wing and sting deflections. Model deflection data must be available to test personnel both during and following each run to aid in assessing whether the model or sting has approached structural limits and to provide the user with information about model deformation and position in the flow for corrections to the aerodynamic data. During the run, the model may undergo programmed changes in the angle of attack in either a continuous or a pitch-pause mode. Therefore, the position of the model relative to fixed reference or relative to another model must be known. Since the measurement system must not disturb the flow, conventional measurement techniques are inappropriate for use in wind tunnels.

A laser interferometric technique is proposed for these measurements based on similar techniques established by others (Refs. 2 through 7). This technique requires only small retroreflectors mounted flush with the model surface as preparation for measurement. Resolution of the proposed technique in measuring absolute or differential displacements is one-quarter of the wavelength of the laser illumination source.

This report describes the two-beam optical system and electronic signal processors developed to implement the technique on an experimental basis. A description of the two-beam and a proposed multiple-beam optical system and an analysis of the salient optical system parameters are presented in Section 2.0. The electronic signal data processors which provide the displacement information are discussed in Section 3.0. The errors inherent in this system attributable to changing laser parameters and the effects of variations in the index of refraction of the airflow are considered in Section 4.0. Section 5.0 summarizes the work completed, and recommendations for future work are presented.

2.0 OPTICAL SYSTEM ANALYSIS

An experimental two-beam optical system has been developed as the basic building block for a proposed multibeam system. This two-beam system provides operating criteria concerning the mixing of light from retroreflectors, retroreflector characteristics, photodetector sensitivity, laser power requirements, and electronic signal processing.

The design of the two-beam system is considered first followed by the design considerations for a multibeam system. Theoretical discussions concerning design parameters which apply to both systems are then given.

2.1 TWO-BEAM OPTICAL SYSTEM

The optical system of the two-beam laser interferometer developed to measure relative or absolute displacements is shown schematically in Fig. 1. Light from a five-milliwatt helium-neon laser is polarization-rotated 90 deg by a half-wave ($\lambda/2$) plate and reflected to a 34-MHz Bragg cell by mirror M_1 . This rotation is necessary to allow the light to pass undeflected through the polarization-sensitive prisms. In passing through this Bragg cell, part of the beam is up-shifted in frequency and the remaining part called the zeroth order is unperturbed. The positive (up-shifted) first-order beam and the zeroth order are reflected to a beam-separating lens system by mirror M_2 . The first order beam is reflected by mirror M_3 and passes through a birefringent (Wollaston) prism where it is reflected by mirrors M_4 and M_5 to a retroreflector located on the test surface.

These latter mirrors (M_4 and M_5) allow the separation and angle between the illumination beams to be easily adjusted. The unmodulated zeroth-order beam is modulated by a second Bragg cell which is driven at 49 MHz and oriented to enhance the positive first-order deflection. This Bragg cell serves to frequency modulate a portion of the light beam producing an overall frequency shift between the two beams of 15 MHz. The zeroth order or unperturbed beam from this Bragg cell is blocked to prevent extraneous frequencies from being generated should it interfere with the other light beams.

Using two Bragg cells, rather than one, to obtain the desired 15-MHz optical carrier facilitates the isolation from the optical carrier frequency of the individual radio frequency (RF) signals required to drive the Bragg cells (Ref. 7). This permits locating the photodetector

and Bragg cells in close physical proximity without introducing cross-talk into the photodetector at the optical carrier frequency.

Mirror M_7 deflects the 49-MHz frequency-shifted beam from the second Bragg cell to a Glan-Air prism and to a second retroreflector. Total internal reflections within the retroreflectors cause the incident polarization vector to be rotated. The two birefringent prisms therefore separate the vertical polarized portions of the returned beams and deflect them to the beam splitter. The two beams are combined by the variable beam splitter and are reflected to the photodiode by mirror M_6 .

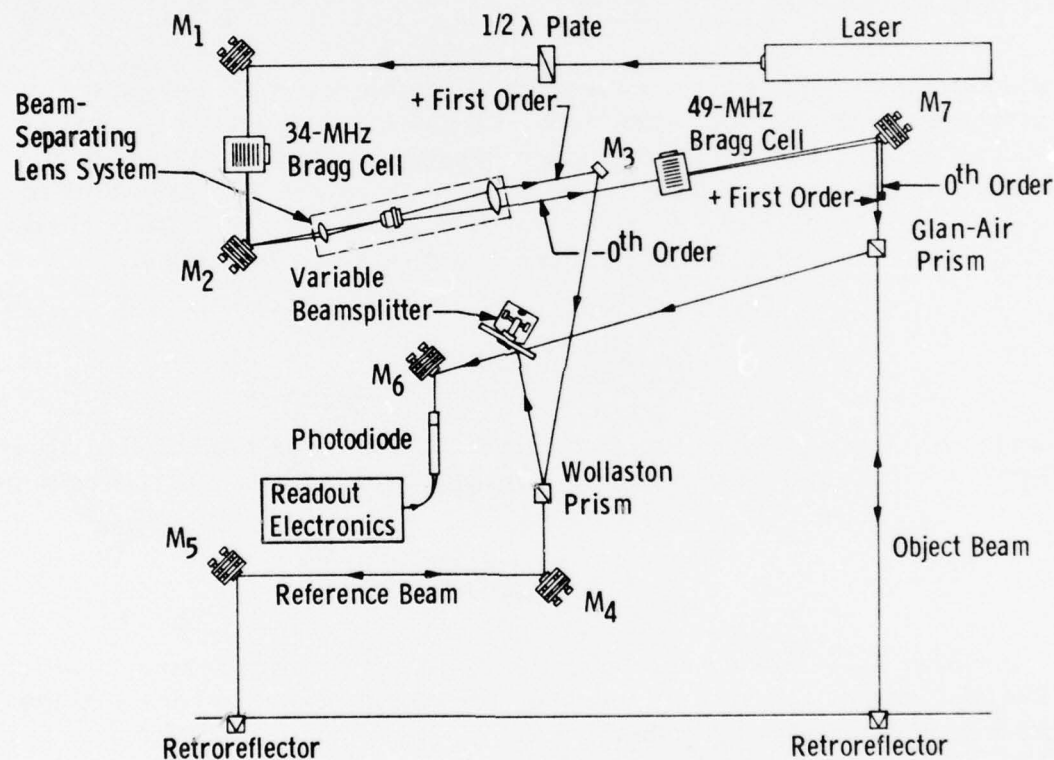


Figure 1. Two-beam optical system schematic.

Mixing or optical heterodyning the two beams at the photodetector can be thought of as establishing virtual fringes, of period $\lambda/2$, normal to the propagation vector of the retroreflector illumination light. Because the two beams are frequency-shifted by 15 MHz, these fringes are moving relative to a stationary reference. Thus the light returned by a stationary pair of retroreflectors will be modulated at 15 MHz.

As a retroreflector moves, the velocity of the reflected fringes will appear to speed up or slow down relative to the direction of motion. This, in turn, is manifested by a change in the signal frequency.

For clarity, the two retroreflector illumination beams will be referred to separately as the object beam and the reference beam, respectively. The output signal from the photodiode, a square-law detector, is proportional to the square of the sum of the incident electric fields, i. e.,

$$i(t) \propto \left\{ E_O \cos [\omega_O t + \phi_O(t)] + E_R \cos [\omega_R t + \phi_R(t)] \right\}^2 \quad (1)$$

where ω_O and ω_R are the frequencies of the object and reference illuminating beams with amplitudes E_O and E_R , respectively, and ϕ_O and ϕ_R are the corresponding phase changes caused by optical path length variations. Both reflector motion, $x(t)$, and the variations in the index of refraction, η , along the optical path due to density changes in the medium are included in these phase terms. In general,

$$\phi = \frac{4\pi}{\lambda} \int \eta \, dx \quad (2)$$

where the integration is along the light path and λ is the wavelength of light in a vacuum. For a constant index of refraction, Eq. (2) becomes

$$\phi(t) = \frac{4\pi}{\lambda} \eta \, x(t) \quad (3)$$

Expanding Eq. (1) and neglecting the optical frequency terms to which the photodiode is unable to respond, the output signal in terms of the measured intensity I is given by

$$i(t) \propto \left\{ I_O + I_R + 2 \sqrt{I_O I_R} \cos \left[\omega_c t + \frac{4\pi}{\lambda} (\eta_O x_O(t) - \eta_R x_R(t)) \right] \right\} \quad (4)$$

where $\omega_c = \omega_O - \omega_R$ is the 15-MHz frequency difference generated by the two Bragg cells, I indicates intensity, and the subscripts, o and R , indicate parameters in the object and reference beams, respectively. The first two terms in Eq. (4) establish a d-c bias at the output of the photodiode on which the phase modulated signal represented by

the third term rides. Phase modulation is manifested on the photodiode signal as a frequency deviation given by

$$\Delta \omega_d = \frac{d\phi}{dt} = \frac{4\pi \eta \Delta v(t)}{\lambda} \quad (5)$$

where $\Delta v(t) = v_o(t) - v_R(t)$, $v_o(t)$ and $v_R(t)$ being, respectively, the components of the object and reference beam retroreflector velocities in the directions along the beam axes and where η is assumed to be constant in time. The effects of variation in the index of refraction generated by flow density variations in the wind tunnels and about the model will be considered in Section 4.2.

2.2 PROPOSED MULTIPLE-BEAM SYSTEM

An optical system proposed to generate and mix multiple light beams for more extensive and detailed interferometric measurements of model deformation and displacement is schematically shown in Fig. 2. The laser light is split into two beams by a Bragg cell positioned to enhance the first order and is driven at 49 MHz. A pair of prisms, P_1 and P_2 , increases the separation between the two beams. The upper beam is down-shifted by 34 MHz by a second Bragg cell resulting in an overall frequency shift between the two beams of 15 MHz. An array of beam splitters and mirrors alternately directs each beam toward a series of polarization-sensitive prisms. (These could be Wollaston, as shown in Fig. 2, or Glan-Air prisms. The ultimate choice will depend on ease of alignment and efficiency in light propagation of the optical system.) All but one of the beams are directed to the model. One light beam is directed toward a reference reflector, M_1 , for an absolute displacement measurement. The rest are directed to the model through small lenses L_1 , of focal length, f_1 , which expand the beams and direct them to a single lens, L_2 , with focal length f_2 . Each small lens is separated from L_2 by $f_1 + f_2$ which results in a collimated output beam with diameter

$$D_o = \frac{f_2}{f_1} d_L \quad (6)$$

where d_L is the beam diameter at L_1 . The small lenses are positioned on a plane parallel to the model to illuminate each area containing a

retroreflector. Their separation, s , in this plane is dictated by the retroreflector separation, S , the focal lengths of the lens system, and the height, H , of L_2 above the model, and is given by

$$s = \frac{(f_1 + f_2)S}{H} \quad (7)$$

Light returned by each reflector is collected and collimated by this same lens system. The resulting beam diameter, d_R , is

$$d_R = \frac{f_1}{f_2} D_R \quad (8)$$

where D_R is the diameter of the effective aperture of the retroreflector. Each beam again enters the polarization-sensitive prisms and because of the polarization rotation within the retroreflectors the perpendicular component is deflected toward the photodetectors.

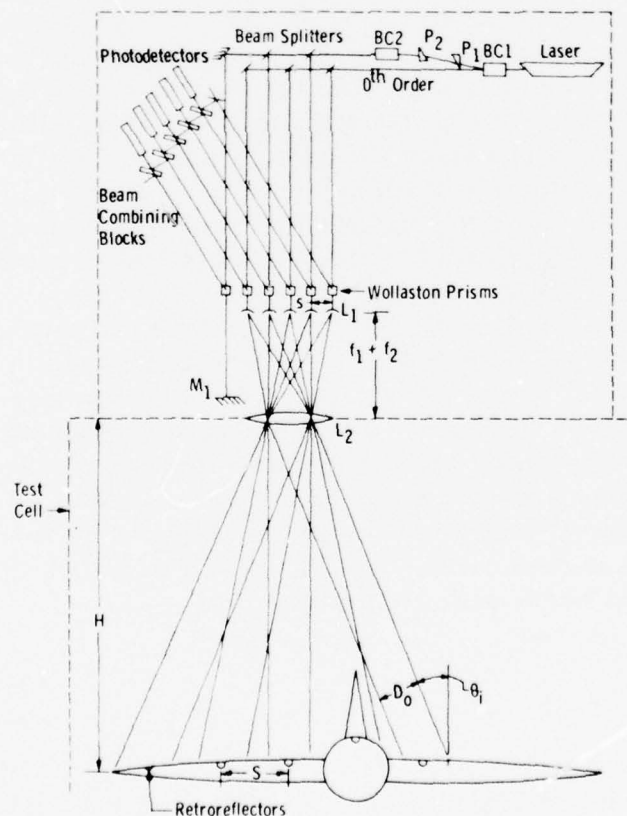


Figure 2. Conceptual multiple-beam optical system.

An array of beam-combining optical blocks mixes adjacent beams and directs them to the photodetectors. To obtain equal intensity beams, the surfaces of these blocks are coated for 50-percent transmission and reflection. Each block functions as two beam-combining elements. This is shown in more detail in Fig. 3. Incident light is reflected by the front surface of one block to the back surface of an adjacent block where it is combined with the light which has passed through that block. Block thickness is chosen to prevent secondary reflections from illuminating the photo-sensitive surface of the detector especially when the model moves laterally. Approximately 50 percent of the light is lost at the beam-combining blocks due to internal reflection and transmission.

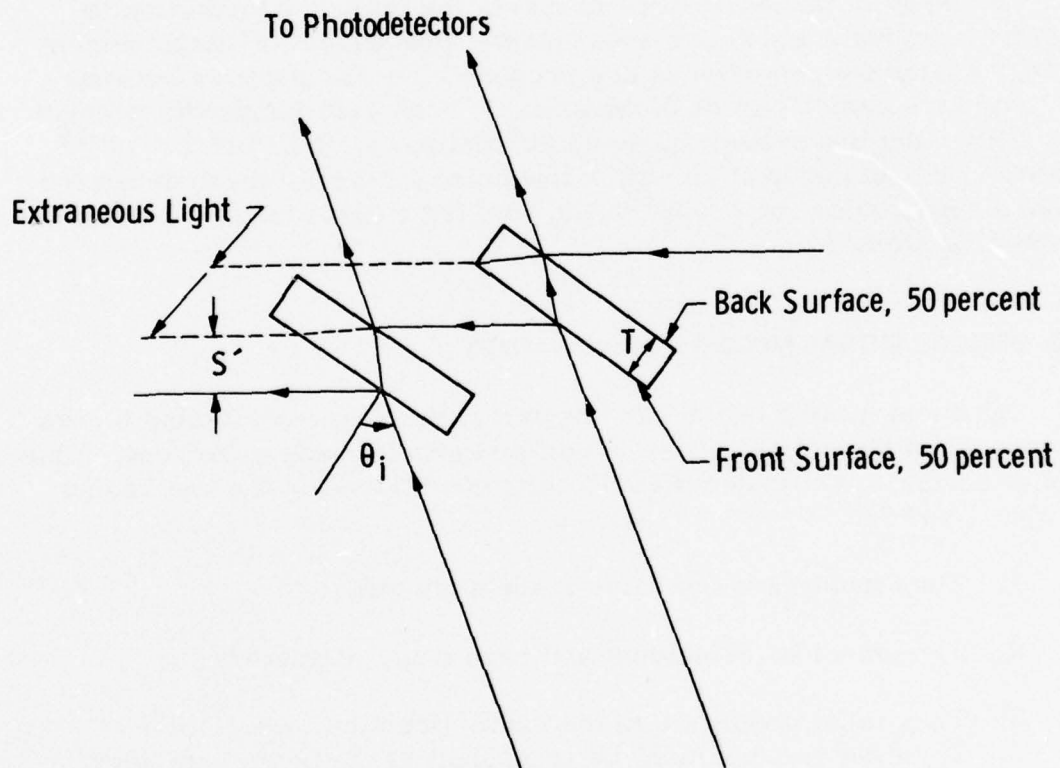


Figure 3. Beam-combining optical blocks.

Lateral motion, L , of the model will cause light returned by the reflector to move across the face of the photodetector. The amount of this motion, ℓ , is given by

$$\ell = \frac{f_1}{f_2} L \quad (9)$$

As an example, if $f_1 = 0.2$ cm and $f_2 = 50$ cm, then $\ell = 4 \times 10^{-3} L$. Therefore, if the reflectors were to move laterally by 5 cm the optical system will reduce this motion at the photodetector to only 0.2 mm. This is an important consideration for angular motion associated with pitch, roll, and angle of attack.

An array of photodetectors converts the optical information to electrical signals which are subsequently processed for displacement data. Avalanche photodiodes are proposed for this purpose because of their high sensitivity (0.2 amps/watt), high gain-bandwidth product (80 GHz), and low system noise equivalent power (NEP) of 2×10^{-13} watts/ $\sqrt{\text{Hz}}$. In conjunction with a low noise amplifier these detectors have a responsivity of 2×10^5 volts/watt for a demodulation bandwidth of 50 MHz (Ref. 8).

2.3 OPTICAL SIGNAL-MIXING REQUIREMENTS

Optimum mixing of the light beams at the beam-combining blocks occurs when the optical phase is uniform across each wavefront. This requirement is met under the following conditions for the two beams (Refs. 7 and 9):

1. They must have the same mode structure,
2. They must be coincident and have equal diameters,
3. They must propagate in the same direction, i.e., their Poynting vectors must be coincident at the beam combiner,
4. Their wavefronts must have the same curvature, and
5. They must be identically polarized.

The first condition is met by using a laser operating in the fundamental (TEM_{00}) mode. The second and third condition can be closely met by fabricating the optical component mounts with the required degrees of freedom for precise beam steering inside the optical package. Focusing at the detector closely achieves similar wavefront curvature at the detector although in a real optical configuration, condition 2 is compromised. The polarization prism ensures optical mixing is achieved with identical polarization vectors. However, as will be seen in Section 4.2, the phase of the returned beams could be distorted by density variations in the flow about the model.

2.4 RETROREFLECTOR ANALYSIS

The retroreflectors (corner cube prisms), which are mounted flush with the surface, reflect the light back to the source over large illumination angles. Thus, as the surface moves due to pitching, rolling, or twisting of the model, optical alignment will not be affected. The intensity, I_R , of the light that is retroreflected, is given by

$$I_R = I_I (1 - \beta) \left(\frac{D_R}{D_o} \right)^2 A(\theta_i) \quad (10)$$

where I_I is the incident intensity, β is the air-glass interface loss due to reflection, D_R is the diameter of the reflector aperture, D_o is the incident beam diameter, and $A(\theta_i)$ is the effective aperture of the corner reflector assuming perfect reflecting surfaces. Figure 4 illustrates the variation of $A(\theta_i)$ for a reflector with a circular aperture and an index of refraction of 1.54 (Ref. 10). The maximum tolerable angle of incidence, θ_i , will depend on the minimum signal level required by the data processing electronics. This in turn is a function of the sensitivity of the photodetector and output noise. Experiments with an avalanche photodiode detector have shown that θ_i can be as much as 32.5 deg before the signal is unacceptable for the electronic signal processor.

Total internal reflection within the retroreflector rotates the orthogonal components of the polarization vector which are parallel and perpendicular to each reflector's plane of incidence. Linearly

polarized light therefore becomes elliptically polarized on total reflection. The amount of rotation, δ , between the two component vectors for a single reflection is (Ref. 11)

$$\tan \frac{\delta}{2} = \frac{\cos \theta_i \sqrt{\sin^2 \theta_i - \eta^2}}{\sin^2 \theta_i} \quad (11)$$

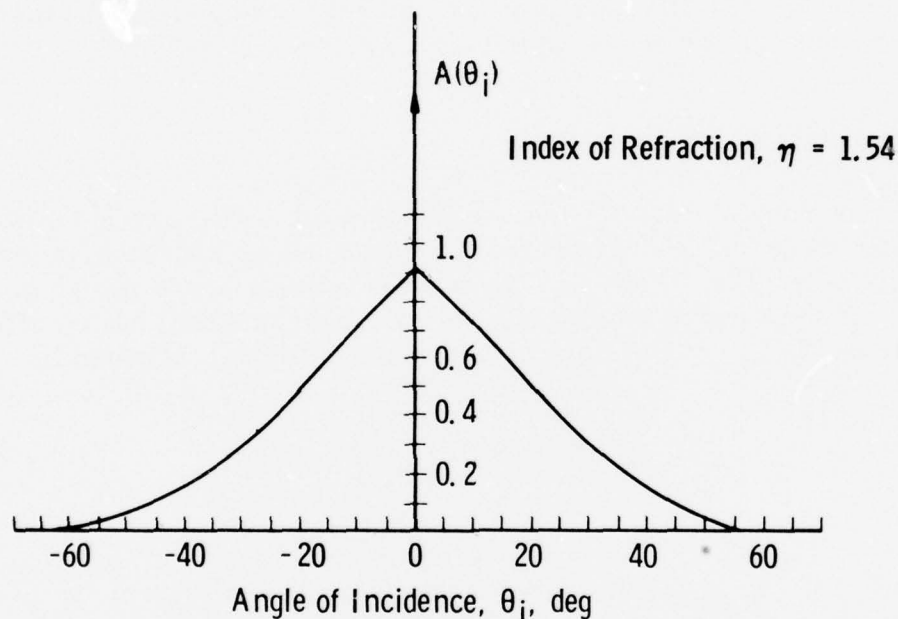


Figure 4. Variation of the effective aperture of a circular retroreflector with angle of incidence.

A maximum δ of 48 deg occurs at an incident angle of 50.4 deg for $\eta = 1.54$. The efficiency of a polarization-sensitive optical system in separating the reflected light from the incident light is therefore not as large as when a mirrored surface is on the object. Compared to a first surface mirror, a retroreflector used in conjunction with a $\lambda/4$ plate and Wollaston prism was found, experimentally, to be approximately 40-percent efficient in returning light to the photodetector. The polarization rotation of the reflectors could be eliminated by coating the reflecting surfaces with silver, thus eliminating the glass-air interface. However, now a $\lambda/4$ plate must be placed between the polarization-sensitive prism and mirror M_4 (Fig. 1) to rotate the polarization vector so that the prism can deflect the returning light to the photodetector.

2.5 ANGULAR MOTION LIMITATIONS

The collimated beams illuminating each retroreflector (Fig. 2) optimize the light returned to the photodetector since areas of the model without a reflector are not illuminated. However, the diameter of each beam, D_o , and the angle of incidence, θ_i , restrict the amount of angular surface motion, α , of each reflector. If the beam diameter is too small, or the illumination angle too large, then a slight rotation can cause the reflector to move out of the illumination and the optical signal will be lost. Four reflector rotation and illumination angle situations which limit surface motion are depicted in Fig. 5. These include illumination (1) normal to the surface, (2) in the direction of rotation, (3) against the direction of rotation, and (4) in the direction of rotation but at a steep angle. The second illumination scheme maximizes the angular rotation while the fourth indicates the severe limits imposed when the angle of incidence is too large. In this case the reflector moves completely out of the opposite side of the illumination beam.

The maximum angular motion of the reflector for cases 2, 3, and 4 is given by

$$\sin \alpha = \sin \theta_i \left(\cos \theta_i - \frac{D_o}{2R} \right) \pm \cos \theta_i \left[\sin^2 \theta_i + \frac{D_o}{R} \cos \theta_i - \left(\frac{D_o}{2R} \right)^2 \right]^{1/2} \quad (12)$$

where θ_i is measured with respect to the surface normal vector and R is the distance of the retroreflector from the axis of rotation, which is assumed to be perpendicular to the plane of the incidence angle. The illumination is also assumed to be centered on the reflector as shown in Fig. 5. For perpendicular illumination ($\theta_i = 0$), Eq. (12) reduces to

$$\cos \alpha = \left(1 - \frac{D_o}{2R} \right) \quad (13)$$

The second term in Eq. (12) is added to or subtracted from the first term depending on whether motion is toward or away from the illumination as shown in Figs. 5b and 5c, respectively. Maximizing the

rotation angle by increasing the illumination angle leads to the limitation shown in Fig. 5d. The maximum illumination angle, θ_m , where the reflector passes tangent to the edge of the beam, is

$$\cos \theta_m = 1 - \frac{D_o}{2R} \quad (14)$$

which is seen to be equal to the maximum rotation angle, α_m , for normal illumination. The angle of rotation at the point of tangency is

$$\sin \alpha = \left[\frac{D_o}{R} \left(1 - \frac{D_o}{4R} \right) \right]^{1/2} \quad (15)$$

As the illumination angle becomes larger than this value, α is limited by the amount of retroreflector travel in the beam before it exits out

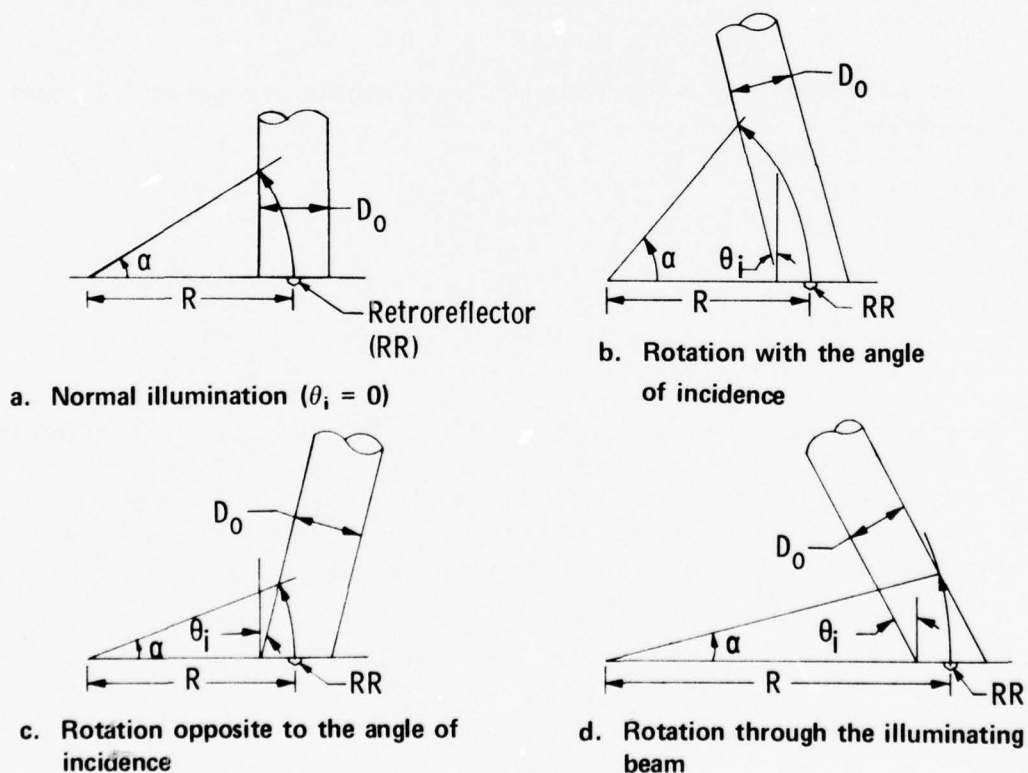


Figure 5. Retroreflector motion within a collimated illumination beam.

of the opposite edge. The angle where it initially leaves the beam is given by

$$\sin \alpha = \sin \theta_i \left(\cos \theta_i + \frac{D_o}{2R} \right) - \cos \theta_i \left[\sin^2 \theta_i - \frac{D_o}{R} \cos \theta_i - \left(\frac{D_o}{2R} \right)^2 \right]^{1/2} \quad (16)$$

Equations (12) and (16) are plotted in Fig. 6 for various values of D_o/R ranging from 0.01 to 0.5. Severe reduction in the rotation angle as the illumination angle increases is quite evident in the figure. As an example, if a wing retroreflector 20 in. from the model center-line is illuminated by a 4-in. -diam beam ($D_o/R = 0.2$) at an incidence angle of 20 deg, then the wing can rotate 53 deg before the reflector leaves the light. However, by increasing the incidence angle to 30 deg

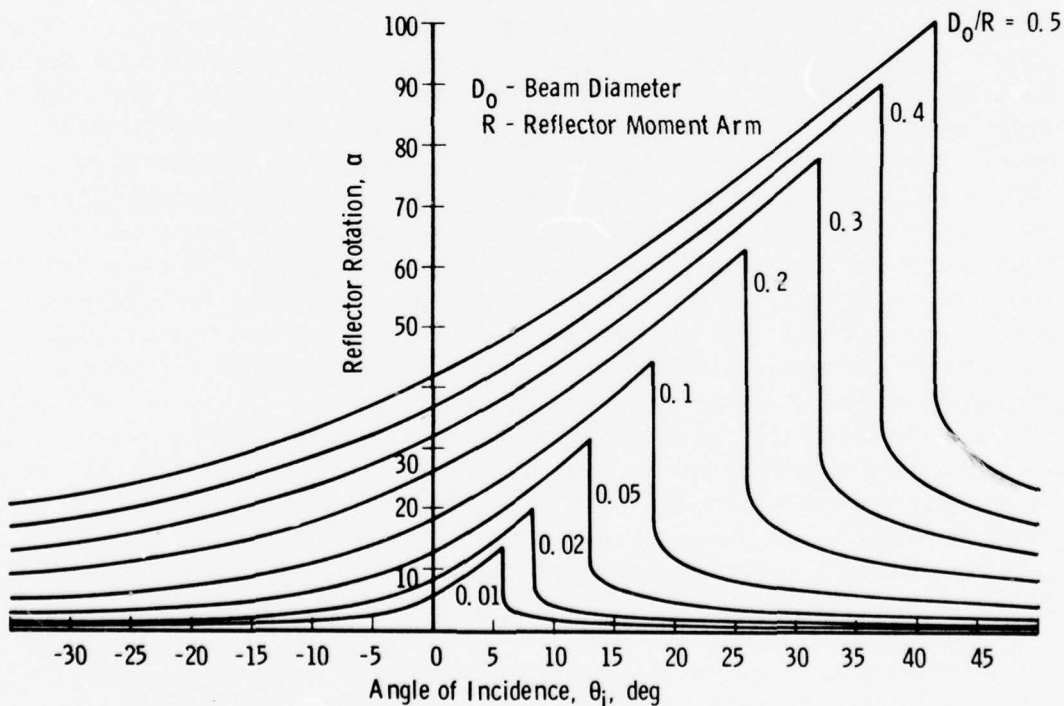


Figure 6. Retroreflector motion within a finite diameter, collimated, illumination beam.

the reflector is restricted to a 15-deg rotation. It should be noted that angle rotations greater than 32 deg will cause a loss in the optical

signal due to the decreasing retroreflector aperture as discussed in Section 2.4. Maximum pitch and roll, therefore, will depend not only on the illumination beam parameters but also on retroreflector placement on the model with respect to the lateral position of the illumination port. By centering the port between the extreme retroreflectors' positions on the model (Fig. 2) the incident angle will be minimized.

Smaller illumination beams and/or larger model rotation can be used in illuminating the model by positioning the light off-center on the retroreflector. However, motion of the reflector must be known a priori. This would be especially advantageous when the model undergoes an initial deflection. D_o in Eqs. (12) to (16) would then be replaced by twice the distance from the reflector to the far edge of the beam.

2.6 LASER POWER AND PHOTODETECTOR SENSITIVITY

The amount of laser power necessary to illuminate the model and be returned to the photodetector depends on the minimum signal-to-noise ratio, SNR, required by the signal processing electronics. The optical signal incident on the detector can be determined by considering the losses incurred by the light as it traverses each optical element. This includes (1) the number, N , of light beams generated; (2) the diameter of the collimated beams, D_o ; (3) the glass-air interface reflection loss, β , for each uncoated optical element (beam splitters are coated to divide the intensity equally among the N beams and the beam splitters are coated for 50-percent transmission and reflection, and all other elements will be assumed to be uncoated); (4) the 50-percent light loss at the beam-combining blocks due to secondary reflections and transmission; (5) the retroreflector light reflecting efficiency which is given by Eq. (10); (6) the efficiency, γ , of the polarization-sensitive prisms in deflecting the light to the photodetector; (7) the efficiency, ϵ , of the second Bragg cell, BC2, in diffracting the light into the first order; (8) the gain, G , of the photodetector at the laser wavelength; and (9) the minimum signal-to-noise ratio required by the signal processing electronics. (Noise on the output signal is due primarily to the inherent noise, N_p , of the photodetector and the optical noise of the light. The latter noise source which is a laser parameter will be neglected.)

The amplitude of the electrical signal out of the photodetector is from Eq. (4)

$$v_s = G \cdot 2 \sqrt{I_i \cdot I_{i+1}} \quad (17)$$

where I_i and I_{i+1} are the intensities of each beam at the photodetector which were generated by Bragg cell, BC1. The two beams are assumed to have equal intensities. Substituting all of the above factors into Eq. (17) yields for the output signal voltage,

$$v_s = 0.5 G \gamma \frac{(1 - \beta)^9}{N} A (\theta_i) \frac{D_R^2}{D_o^2} \sqrt{(1 - \beta) \epsilon} I_L \quad (18)$$

where I_L is the initial laser intensity.

The minimum signal-to-noise ratio, SNR, required out of the photodetector is found by dividing this equation by the noise voltage generated by the photodetector which is given by

$$V_N = (NEP) G \sqrt{\Delta f} \quad (19)$$

where NEP is the noise equivalent power at the input of the photodetector measured in watts-Hz^{-1/2} and Δf is the bandwidth of the circuit. Dividing Eq. (18) by (19) and solving for I_L yields

$$I_L = \frac{(SNR) \cdot N \cdot D_o^2 \cdot (NEP) \sqrt{\Delta f}}{0.5 \gamma (1 - \beta)^9 A (\theta_i) D_R^2 \sqrt{(1 - \beta) \epsilon}} \quad (20)$$

Table 1 lists the laser power required and the values of the parameters in Eq. (20) which were assumed for two illumination beam diameters. The values of I_L are surprisingly low. This is a result of the high sensitivity and low noise of the avalanche photodiode assumed for the photodetector. Under actual operating conditions, optical and electrical noise can be expected to increase the required power. However, by antireflection coating the optical elements and silvering the retroreflectors the required laser power can be minimized.

3.0 DISPLACEMENT INTERFEROMETER SIGNAL PROCESSORS

The output signal from the photodetector is a 15-MHz carrier that has been frequency-modulated by the relative velocity, $\Delta v(t)$, between

the two retroreflectors. The signal frequency from Eq. (4) is

$$f(t) = f_c + \frac{2\eta\Delta v(t)}{\lambda} \quad (21)$$

Two techniques exist for recovering displacement information from this frequency modulation. One is digital and can best be described from a fringe counting point of view. This approach is discussed in Section 3.1. The second technique is analog and involves converting the signal frequency to proportional analog voltage which, after subtracting a constant corresponding to the 15-MHz carrier, can be integrated to obtain displacement. This type signal processor is discussed in Section 3.2. Section 3.3 describes experiments run to compare results obtained with both type signal processors.

Table 1. Multiple-Beam Optical System Parameters and Required Laser Power

$$\text{SNR} = 100$$

$$(1-\beta) = 0.90$$

$$\gamma = 0.65 \text{ (polarization-sensitive prism deflection efficiency)}$$

$$A(\theta_i) = 0.50 \text{ } (\theta_i = 20 \text{ deg from Fig. 4})$$

$$D_R = 0.25 \text{ in. (retroreflector diameter)}$$

$$\epsilon = 0.75 \text{ (Bragg cell No. 2 diffraction efficiency)}$$

$$\text{NEP} = 5 \times 10^{-13} \text{ W/(Hz)}^{1/2} \text{ (from Ref. 8 for a TIXL74 avalanche photodiode module)}$$

$$\Delta f = 10 \text{ MHz}$$

$$N = 10$$

$$D_o = 4 \text{ in.}$$

$$D_o = 2 \text{ in.}$$

$$I_L = 7.8 \text{ mW}$$

$$I_L = 2.0 \text{ mW}$$

3.1 PHASE QUADRATURE DIGITAL DATA PROCESSOR

This approach to processing the photodetector signal uses a digital up/down counter to measure surface position by counting digital pulses developed for each plus or minus $\lambda/4$ of surface motion. Knowledge of when the surface changes direction is needed to accurately track surface position by directing $\lambda/4$ pulses to the appropriate up or down counter terminal. A pulse separation circuit which utilizes the phase difference between the Bragg cell and photodiode signals to instantaneously separate up and down position pulses will be described.

Figure 7 is a block diagram of the circuit used to digitally process the photodetector signal. Not shown are the 34- and 49-MHz crystal oscillators used to drive the Bragg cells. The 15-MHz frequency-modulated (FM) signal, $S(t)$, from the photodetector, and the 34-MHz, $d_1(t)$, and 40 MHz, $d_2(t)$, signals which drive the Bragg cells to produce the 15-MHz frequency difference between the object and the reference light beams are the circuit inputs. These can be represented by

$$\begin{aligned} S(t) &= V_0(t) \cos \left[\omega_{15} t + \frac{4\pi}{\lambda} \Delta x(t) \right] \\ d_1(t) &= V_1 \cos [\omega_{34} t] \\ d_2(t) &= V_2 \cos [\omega_{49} t] \end{aligned} \tag{22}$$

where the subscripts on ω indicate the frequency value in megahertz and assuming $\eta = 1$. The amplitude of $S(t)$ is shown as a function of time due to the change in incident angle and subsequently a change in the returned light amplitude from the retroreflector as the model moves. Limiter, A_2 , provides a constant signal amplitude for V_0 . The 34- and 49-MHz signals are multiplied together by a double-balanced mixer to give sum and difference frequencies, i. e.,

$$g(t) = \frac{V_1 V_2}{2} \cos (\omega_{15} t) + \frac{V_1 V_2}{2} \cos (\omega_{83} t) \tag{23}$$

A 20-MHz lowpass filter removes the high frequency component and an amplifier, A_3 , separates the 15-MHz reference signal into two complementary signals 180 deg out of phase. The phase of the noninverted signal is decreased 90 deg by a delay line so that the total phase shift

between the two is 90 deg. These signals can be represented as

$$\begin{aligned} r_1(t) &= \frac{V_1 V_2}{2} \cos(\omega_{15} t - \pi) \\ r_2(t) &= \frac{V_1 V_2}{2} \cos(\omega_{15} t - \pi/2) \end{aligned} \quad (24)$$

Two double-balanced mixers multiply these signals with the photodetector signal, $S(t)$, to produce $M_1(t)$ and $M_2(t)$, respectively, which after algebraic and trigonometric simplification, can be expressed as

$$\begin{aligned} M_1(t) &= \frac{V_0 V_1 V_2}{4} \left[\cos\left(\omega_{30} t + \frac{4\pi}{\lambda} \Delta x(t)\right) + \cos\left(\frac{4\pi}{\lambda} \Delta x(t)\right) \right] \\ M_2(t) &= \frac{V_0 V_1 V_2}{4} \left[\sin\left(\omega_{30} t + \frac{4\pi}{\lambda} \Delta x(t)\right) - \sin\left(\frac{4\pi}{\lambda} \Delta x(t)\right) \right] \end{aligned} \quad (25)$$

Lowpass filtering the output from each of the mixers removes the 30-MHz frequency term and yields

$$P_1(t) = \frac{V_0 V_1 V_2}{4} \cos\left(\frac{4\pi}{\lambda} \Delta x(t)\right) \quad (26a)$$

$$P_2(t) = \frac{V_0 V_1 V_2}{4} \sin\left(\frac{4\pi}{\lambda} \Delta x(t)\right) \quad (26b)$$

Note that the delays in the filters are matched since subsequent signal processing will depend on the phase between these two signals. Also, note that the 5-MHz break frequency of these filters limits the maximum allowable surface velocity to ± 1.6 meters/sec.

It can be seen from Eq. (26) that $P_1(t)$ has the same sign regardless of the sign of $\Delta x(t)$, which changes with the surface direction. However, when the sign of $\Delta x(t)$ changes, the sign of $P_2(t)$ also changes and it is this signal in conjunction with $P_1(t)$ that is used to direct position pulses to the up or down terminal of the counter.

Signals P_1 and P_2 are converted to Transistor Transistor Logic (TTL) pulse trains, A and C, respectively, in Fig. 7 by zero-crossing detectors A_4 and A_5 . Delaying each signal by 15 and 30 nsec yields TTL

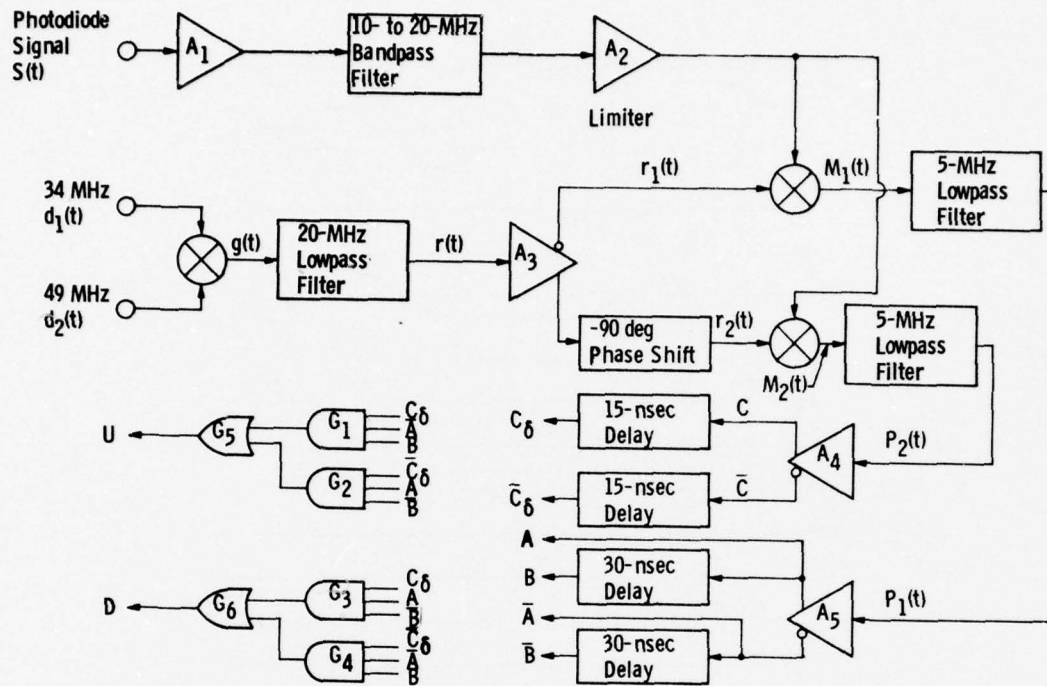


Figure 7. Phase quadrature position data processor.

pulse trains C_δ and B , respectively. The AND gates, G_1 to G_4 , and OR gates, G_5 and G_6 , implement the Boolean logic expressions

$$U = \bar{A} \cdot B \cdot C_\delta + A \cdot \bar{B} \cdot \bar{C}_\delta \quad (27a)$$

$$D = \bar{A} \cdot B \cdot \bar{C}_\delta + A \cdot \bar{B} \cdot C_\delta \quad (27b)$$

where \bar{A} , \bar{B} , and \bar{C}_δ are the Boolean complements of the A , B , and C_δ pulse trains, respectively. These expressions generate position pulses on either the up or down line (U or D expression, respectively) of the counters depending upon the direction of the surface motion. Each position pulse is 30 nsec wide and is produced for each $\lambda/4$ of surface movement.

The operation of this logic circuit (and the Boolean expressions) in detecting the phase between the two signals can be understood by analyzing the time sequence of the waveforms shown in Fig. 8. The Boolean logic identity $A \cdot B \cdot C = (A \cdot B) \cdot C$ will be utilized to show how the 30-nsec pulsewidths are generated. It is seen in Fig. 8 that the logical multiplications (AND operations) of A with \bar{B} and of \bar{A} with B result in

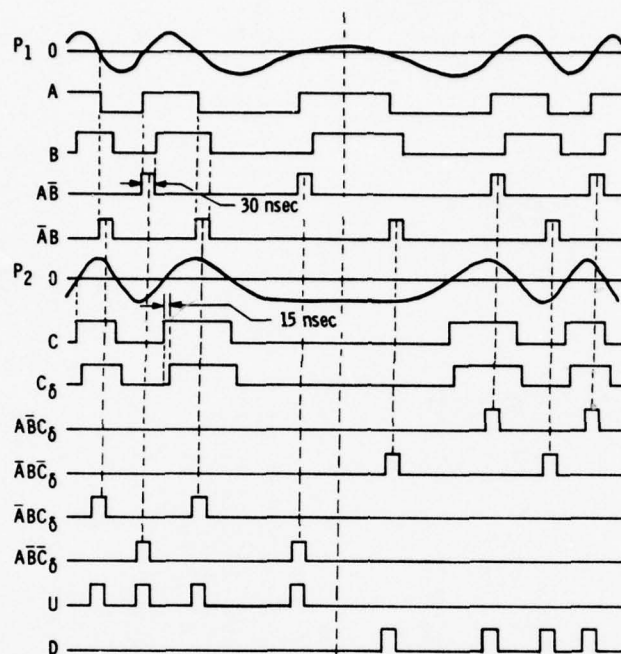


Figure 8. Analog waveforms and logic pulse trains for the phase quadrature signal processor.

30-nsec pulses which occur at the positive and negative going zero crossings, respectively, of the P_1 waveform. These position pulses are then separated according to the logic state of C since, according to Eq. (26b), the sign of P_2 and therefore the logic state of this signal is dependent on the sign of $\Delta x(t)$. (Note that the C pulse train is delayed by 15 nsec to best center C_δ and the 30-nsec position pulses in order to optimize frequency response.)

To fully evaluate the pulse separation circuit just described, it is necessary to verify that no pulses are lost or gained on the U or D logic line at surface turnaround for each possible phase relationship between the A and C waveforms. As explained earlier, the surface can be assumed to be cutting virtual fringes with P_1 and P_2 , the representative expressions for the resulting signals. Therefore, a physical understanding of the effects of surface motion and, correspondingly, the phase difference between P_1 and P_2 on the position pulses preceding and following a direction change at various locations in this fringe pattern can be obtained. Figure 9 illustrates zero crossings of P_1 (solid lines) and P_2 (dashed lines) along the light propagation path, z . Paths 1 through 4 indicate four possible phase relationships between the logic signals A and C at the turnaround point. These signals and the resulting pulse

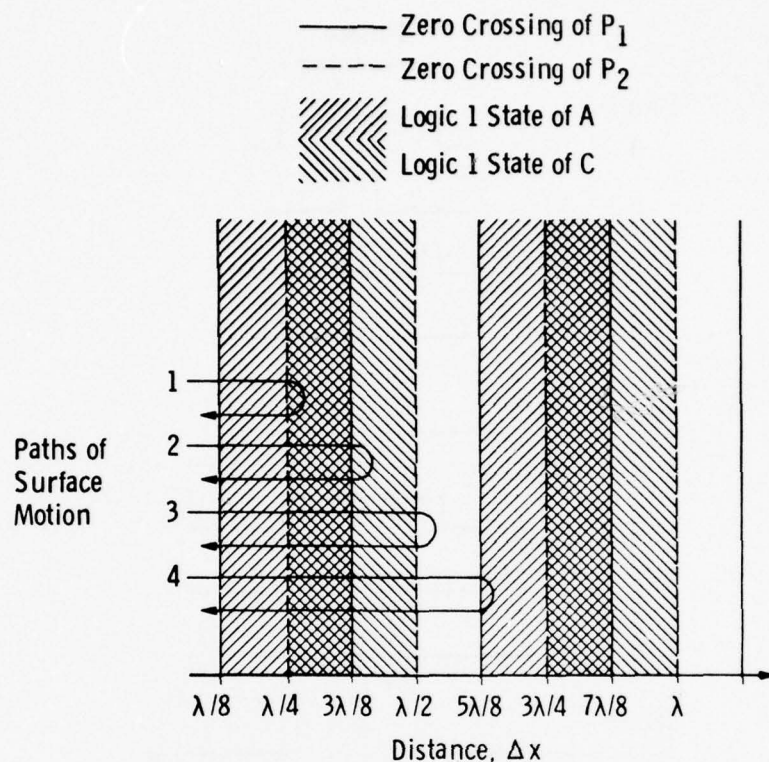


Figure 9. Pictorial representation of surface motion-generating phase-delayed signals P_1 and P_2 .

trains on the up and down counting busses for paths 1, 2, and 3 are illustrated in Fig. 10. Signals for the fourth path correspond to those presented in Fig. 8 as a function of time. In Fig. 10 the signals have been shifted for coincident turnaround points. A symmetrical count is observed in all instances, i.e., there are as many pulses on the up logic line as there are on the down line for equidistant motion.

Noise on the input signal $S(t)$ can affect the count through the A and C waveforms by adding or dropping pulses from the waveforms. Pulse addition could result in erroneous counts being accumulated. However, the probability of pulse addition or cancellation occurring with this circuit is small. For example, if a noise pulse occurred in the A waveform while the C waveform remained either a logic 1 or a logic 0, one up and one down count pulse would be generated. The overall effect of the noise pulse would therefore be zero. A $\lambda/4$ error would occur in the data only if the contents of the counters were recorded between the rising and falling edges of the added pulse. A similar argument holds for pulse cancellation. Only when the addition or cancellation of a pulse by noise occurs

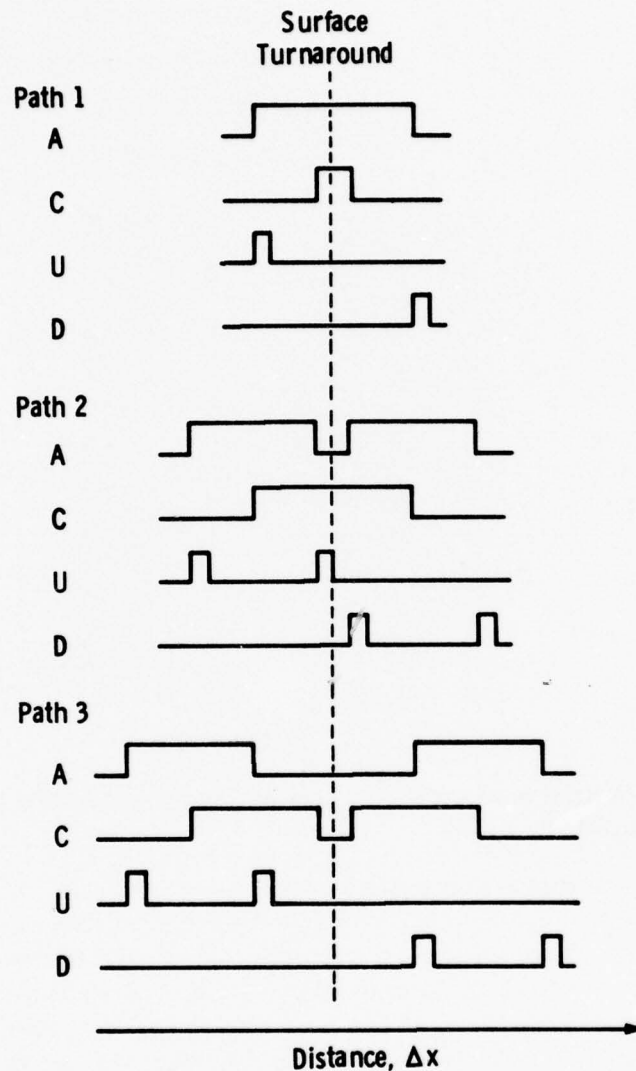


Figure 10. Logic waveforms of surface motion depicted in Fig. 9.

on A at the same time as a state transition on C or vice versa will erroneous counts be unequally accumulated. The amount of this error would then be a function of the input signal-to-noise ratio. Noise pulses on the C waveform could cause a position pulse to be on the wrong counter input only if it occurred at the same time as the position pulse and was at least 30 nsec wide.

Resolution of the displacement data can be reduced from $\lambda/4$ to $\lambda/2$ thus reducing the number of logic circuit components required and

doubling the maximum surface velocity capability of the logic circuitry. This is accomplished by implementing only one term from each of the expressions in Eq. (27). Of the four possible combinations for the U and D functions, only two

$$U = \bar{A} \cdot B \cdot C_{\delta}, \quad D = A \cdot \bar{B} \cdot C_{\delta} \quad (28)$$

and

$$U = A \cdot \bar{B} \cdot \bar{C}_{\delta}, \quad D = \bar{A} \cdot B \cdot \bar{C}_{\delta} \quad (29)$$

are appropriate. The other two pairs have the possibility of a pulse being dropped each time the surface changes direction. As an example, referring to the waveforms in Fig. 8, and assuming that the logic expressions $U = \bar{A} \cdot B \cdot C_{\delta}$ and $D = \bar{A} \cdot B \cdot \bar{C}_{\delta}$ are to be implemented, the phase relationship of signals A and C is such that a position pulse is not present on the up input since, prior to surface turnaround, the A waveform is in a high logic state. The expressions of Eqs. (28) and (29) on the other hand are consistent in generating both an up and a down pulse when the surface changes direction.

A pulse separation circuit implementing both terms of Eq. (27) to obtain $\lambda/4$ resolution was fabricated. Presented in Fig. 11 are photographs of circuit waveforms taken from an oscilloscope to verify proper circuit operation. Figure 11a shows $P_1(t)$ and $P_2(t)$ at a surface turnaround point (horizontal screen center) along with their corresponding TTL logic waveforms, A and C. Figure 11b illustrates formation of the term $A \cdot \bar{B} \cdot C_{\delta}$ from Eq. (27). Figure 11c illustrates the transfer of position pulses between the up and down counter lines at surface turnaround.

It is interesting to note that this data processing technique is similar in operating principle to the optical quadrature technique which utilizes two photodetectors optically separated by 90 deg on the interference pattern (Ref. 12). However, the electrical circuit requires half as many photodetectors and is not sensitive to photodetector position.

3.2 ANALOG DATA PROCESSOR

An analog approach used to determine position from the frequency-modulated photodetector signal involves converting the signal frequency to a proportional analog voltage, removing from it a constant voltage proportional to the carrier frequency, f_c , and integrating. The problem with this approach occurs in trying to obtain frequency-to-voltage conversion at 15 MHz while still maintaining the accuracies required. A

solution to this problem utilizes frequency scaling to move the photo-detector signal to a lower frequency range which is compatible with standard and very accurate frequency-to-voltage (f/v) converters.

The converter used in the prototype analog processor decodes frequencies ranging from 10 Hz to 110 kHz to voltages between 1 mv and 11 v, respectively. Typical linearity is ± 0.006 percent with a maximum tolerance of ± 0.05 percent. The converter time constant is 0.05 msec which results in less than a 0.008 percent amplitude variation of output voltage at frequencies between 0 and 100 Hz.

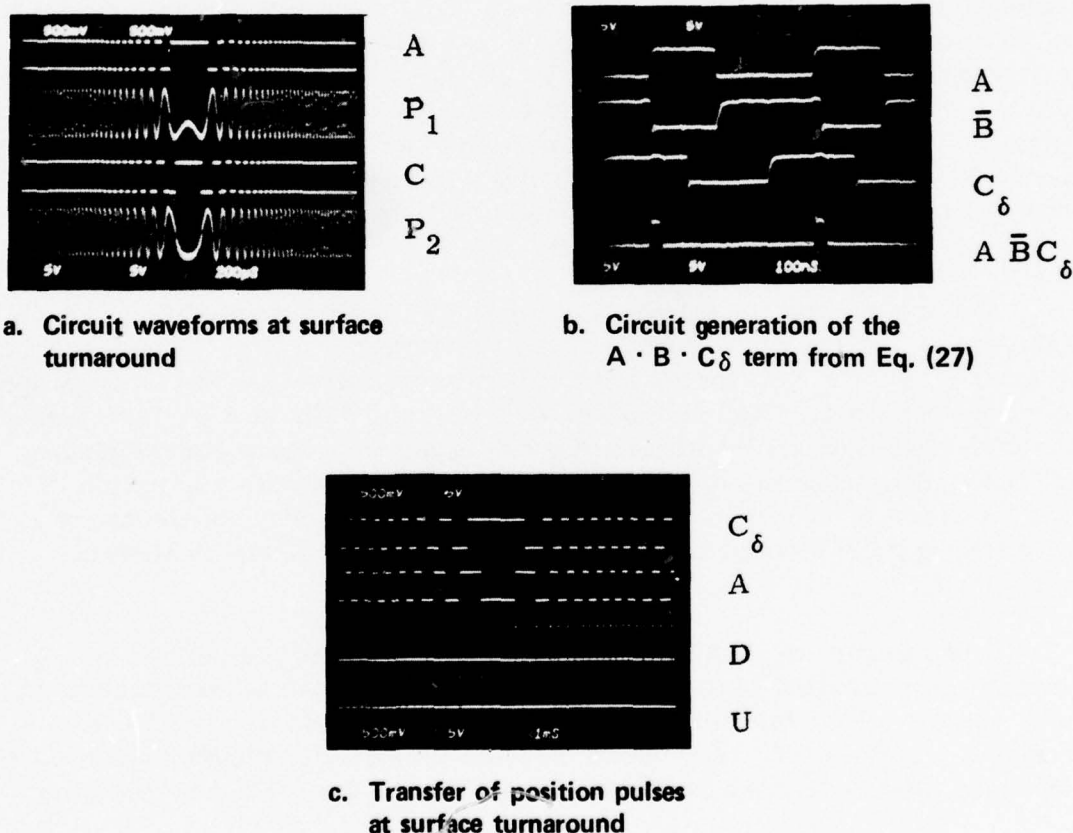


Figure 11. Circuit waveforms from the $\lambda/4$ resolution digital processor.

Figure 12 is a block diagram of the analog position measurement system. The amplitude-limited (by limiter A_2), bandpass-filtered FM signal is frequency-translated to 55 kHz, the center frequency of the f/v converter. It is simultaneously scaled so that the range of frequency variations, Δf , does not exceed the full-scale range of the converter. Frequency translation is achieved by heterodyning this signal with a

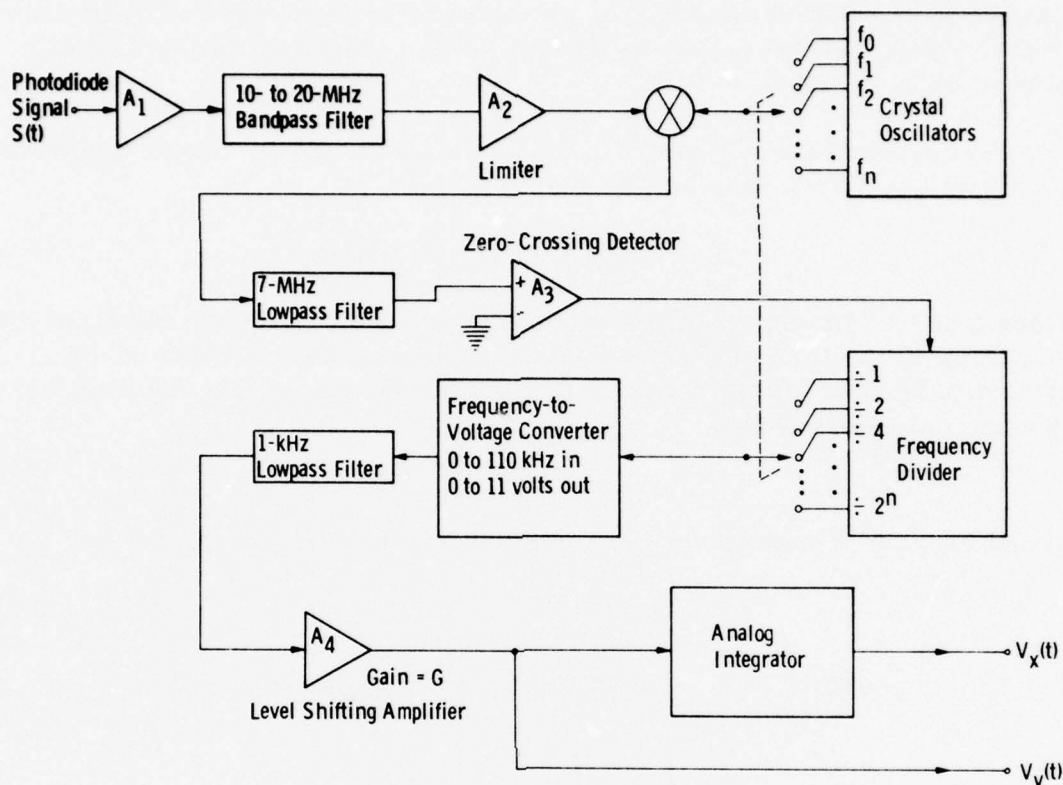


Figure 12. Analog readout, frequency-to-voltage converter.

higher frequency crystal-controlled oscillator signal of frequency f_n . The sum frequency component is removed from the difference frequency by a lowpass filter. An oscillator higher in frequency than 15 MHz is used because it gives a greater separation between the sum and difference frequencies than would a lower frequency oscillator, thus easing the rolloff requirements on a lowpass filter. However, the higher frequency oscillator produces an inversion in the direction of frequency deviation of the translated FM signal. The output from the lowpass filter is converted to a TTL compatible signal by zero-crossing detector A_3 . Frequency scaling is then performed by digital division with a chain of flip-flops.

The amount of frequency translation and division can be optimized to the full range of the f/v converter with respect to the maximum surface velocity expected. This allows the sensitivity of the technique to be maximized. However, 55 kHz minus the sum of the highest modulating frequency (5 kHz) and the maximum value of Δf must always be

positive if the displacement information is to be recovered without distortion. This requirement can be met here by limiting the maximum allowed value of Δf to 50 kHz.

Frequency translation and division with a resultant center frequency of 55 kHz can be represented by the equation

$$(f_n - 15 \text{ MHz})/2^n = 55 \text{ kHz} \quad (30)$$

where n is the number of flip-flops in the frequency divider and f_n is the frequency of the translation oscillator. The requirement that Δf be limited to 50 kHz following frequency division dictates (for the maximum frequency deviation) that

$$\Delta f_{\max} = 2^n \cdot 50 \text{ kHz} \quad (31)$$

Since Δf_{\max} is a function of peak surface velocity, v_{\max} , given by

$$\Delta f_{\max} = (2/\lambda) v_{\max} \quad (32)$$

Equation (31) can be solved for n in terms of v_{\max} and λ yielding

$$n = \left[\left[\frac{\log \left(\frac{2 v_{\max}}{\lambda \cdot 5 \cdot 10^4} \right)}{\log 2} \right] \right] \quad (33)$$

where $\left[\left[\right] \right]$ indicates that n is the next greater integer of the value in these symbols. After determining n , f_n is obtained from Eq. (30) where

$$f_n = (2^n \cdot 55 \text{ kHz}) + 15 \text{ MHz} \quad (34)$$

As an example, assume that the maximum expected velocity is 1 m/sec. Substituting into Eq. (33) with $\lambda = 6328 \text{ \AA}$ gives

$$\eta = \left[\left[5.98 \right] \right] = 6$$

Using this value of n in Eq. (34) gives a value for f_n of 18.520 MHz. The frequency deviation from 15 MHz for a velocity of 1 m/sec is, from Eq. (32), 3.16 MHz. This means that the largest desired frequency out

of the balanced mixer is the difference between 18.52 MHz and 11.84 MHz (15 MHz minus 3.16 MHz) or 6.68 MHz. The break frequency of the low-pass filter should then be greater than 6.68 MHz with high attenuation near 30 MHz in order to reject the sum frequency from the balanced mixer output.

Additional ranges with full-scale velocities of 0.5 m/sec, 0.25 m/sec, etc. can also be made available as shown in Fig. 12 by switching in different frequency translation oscillators (16.76 MHz, 15.88 MHz, etc.) and correspondingly different values of n (5, 4, etc.). Maximum sensitivity occurs on the range where $n = 0$ and $f_n = 15.055$ MHz. Here a velocity of only ± 1.75 cm/sec produces a full-scale output of 10 v from the frequency-to-voltage converter. Conversely, values of n larger than six with a higher value for the filter break frequency and with higher frequencies for f_n would permit full-scale velocities greater than 1 m/sec if required.

The output of the frequency-to-voltage converter is lowpass-filtered to reduce noise on the velocity-analog signal. For the type of FM demodulation system used, the total system noise bandwidth is that of this filter (assuming acceptable input FM signal-to-noise ratios) (Ref. 13). This filter also reduces ripple at the converter input frequency which appears on the output and, although in the millivolt range, can contribute an error into the integrated data.

Care must be taken to ensure that the filter response does not roll off significantly, and, in turn, vary the amplitude of analog voltages having frequency components below the maximum expected displacement frequency component (typically 100 Hz). The rolloff effects of various practical filters were analyzed with a computer. An inductor-capacitor (LC) pi filter with a break frequency of approximately 1 kHz and with a 1-k Ω termination impedance was found to be the best of those studied. A practical 0.3-h inductor having 35 ohms of series resistance, and a pair of 0.15- μ f capacitors in this configuration were found to vary the amplitude by only 0.015 percent below 100 Hz while providing more than 40 db of attenuation above 5 kHz. Insertion loss in the filter was calculated to be 1.72 percent.

Operational amplifier (op-amp) A_4 (Fig. 12) removes the d-c term corresponding to the 55-kHz translated value of the 15-MHz carrier and provides inversion so that the polarity of the voltage into the integrator corresponds to the direction of motion. Additionally, since the analog integrator will normally accept full-scale inputs different from the full-scale output of the converter and because of signal attenuation in the

filter termination network, the amplifier gain is adjusted to optimize and calibrate the analog circuit.

Calibration of the analog measurement system for values of n and f_n is simply a matter of adjusting the gain of op-amp A_4 to a convenient value. This can be done with a frequency counter, signal generator, and voltmeter. If the filter and op-amp are considered to have a composite gain of G' , the governing calibration equation is

$$\Delta v(t) = \left[\frac{2^{n-1} \cdot \lambda \cdot 10^4}{G'} \right] V_v(t) \quad (35)$$

for the velocity signal where $V_v(t)$ is the voltage out of op-amp A_4 , and

$$\Delta x(t) = \left[\frac{2^{n-1} \cdot \lambda \cdot 10^4}{G_I G'} \right] V_x(t) \quad (36)$$

for the displacement signal. $V_x(t)$ is the voltage at the output of the integrator and G_I is the integrator gain.

A prototype analog data processor was fabricated with five full-scale velocity ranges of from ± 1.6 cm/sec to ± 1 m/sec, each of which provides a ± 10 -v output at full scale. To verify proper operation of the processor, the 15-MHz-centered frequency-to-voltage conversion characteristic of each range was checked with a signal generator, frequency counter, and digital voltmeter. In each case the characteristic proved to be a straight line within the measurement accuracy of the 3.5-digit voltmeter used. The frequency response of the output lowpass filter was also checked and found to agree with the desired theoretical response.

3.3 EVALUATION OF DIGITAL AND ANALOG PROCESSORS

An experiment was conducted comparing the phase quadrature digital readout unit to a known standard. A 4-in.-diam micrometer with a 1-in. travel was used to push a gauge block having a retroreflector attached. The results were as expected with the digital readout giving the correct value for the micrometer reading to a better resolution than could be obtained from the micrometer scale.

The analog readout was calibrated against a known frequency deviation and a frequency-to-voltage factor established as discussed in the previous section. To further evaluate the two-beam system, a comparison between the two different readout techniques was undertaken.

To experimentally compare the performance of the digital and analog data processors, displacement measurements were taken of a vibrating bar (Fig. 13) as a simulation of model motion in a wind tunnel. The bar was mounted horizontally on a small optical bench such that its length could be varied to change the natural frequency of oscillation. An initial displacement was set with a standoff holding the bar from the neutral position. Varying the length of the standoff gave free choice of the initial displacement. Rapid removal of the standoff set the bar oscillating about the neutral position. Judicious addition of weight to the bar allowed some control of the oscillating frequency and its harmonic modes. Near the free end, a 0.5-in. retroreflector was mounted with the option of mounting the other retroreflector on the oscillating bar or fixing it to a stationary reference.

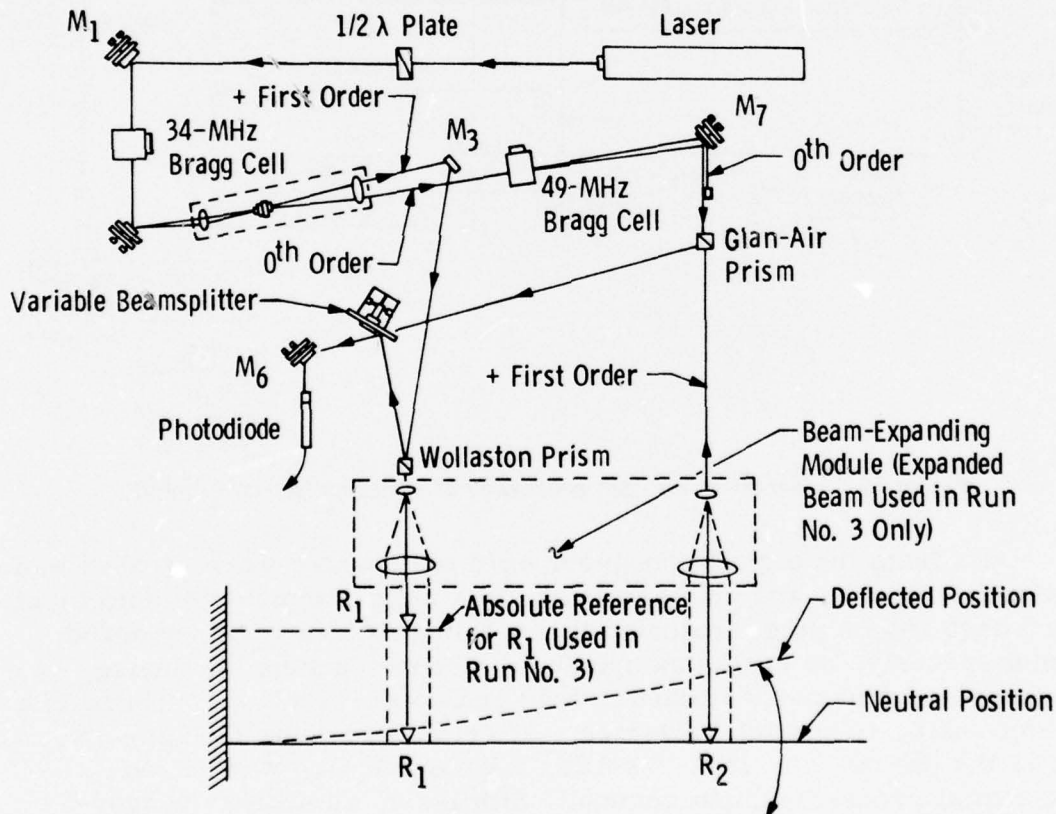


Figure 13. Experimental setup for the vibrating bar experiment.

Data from the two processors were recorded simultaneously with a minicomputer data acquisition system. Pairs of readings were taken at fixed intervals of time as determined by a gated pulse generator. A flow

chart is shown in Fig. 14 describing the data acquisition. At the beginning of each data run, the computer would await a command pulse from the pulse generator to record the first pair of data points. The pulse generator was gated ON just prior to removing the standoff holding the deflected bar. The computer then recorded data in pairs each time a pulse was generated until the required number of points for the run had been obtained.

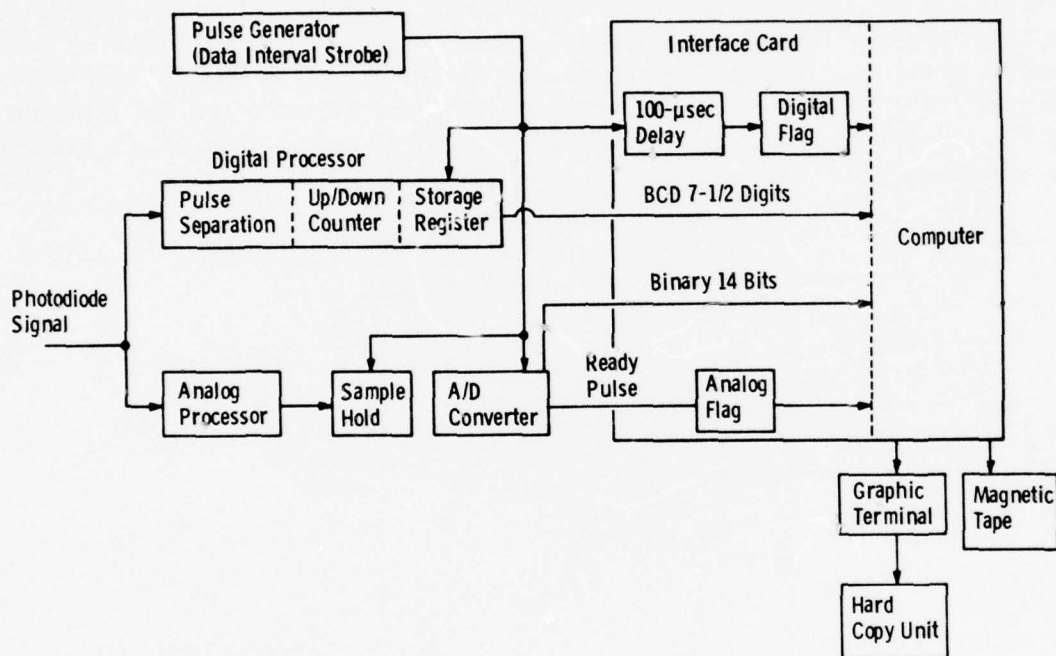


Figure 14. Flow chart for data processing of vibrating bar experiment.

Data from the digital processor up/down counter were strobed into a storage register and made available to a computer parallel data input card each time a pulse indicated that a data pair was to be recorded. Simultaneously, an analog sample/hold circuit tracking the analog processor output was switched to hold and conversion was initiated in a 14-bit analog-to-digital converter. After a short delay (100 μ sec) to allow the digital data lines to settle, a computer flag was set on the digital processor input channel. Similarly, as soon as conversion of the analog reading was completed, a flag was set on the analog data channel. When both flags were set, the data pair was stored as equally indexed elements of two memory arrays reserved for the respective processors. Since storage of the data pair required less than 30 μ sec, the maximum rate at which data pairs

could be taken (i. e., the maximum frequency to which the pulse generator could be set) was essentially determined by the digital data line setting delay of 100 μ sec. Sample rates of up to 10 kHz were therefore possible although most of the data taken were recorded at rates of 500 Hz or less.

Memory arrays for the data were reserved by a supervisory BASIC language program. After setting up the array allocation, the BASIC program transferred control to an assembly level subroutine. This subroutine acquired the data in pairs each time the two flags were set. Once the pulse generator was gated ON and the number of pairs requested by the BASIC program was obtained, the assembly routine converted the data to the format required by the BASIC compiler. The arrays and control were then returned to the supervisory BASIC program for all further operations.

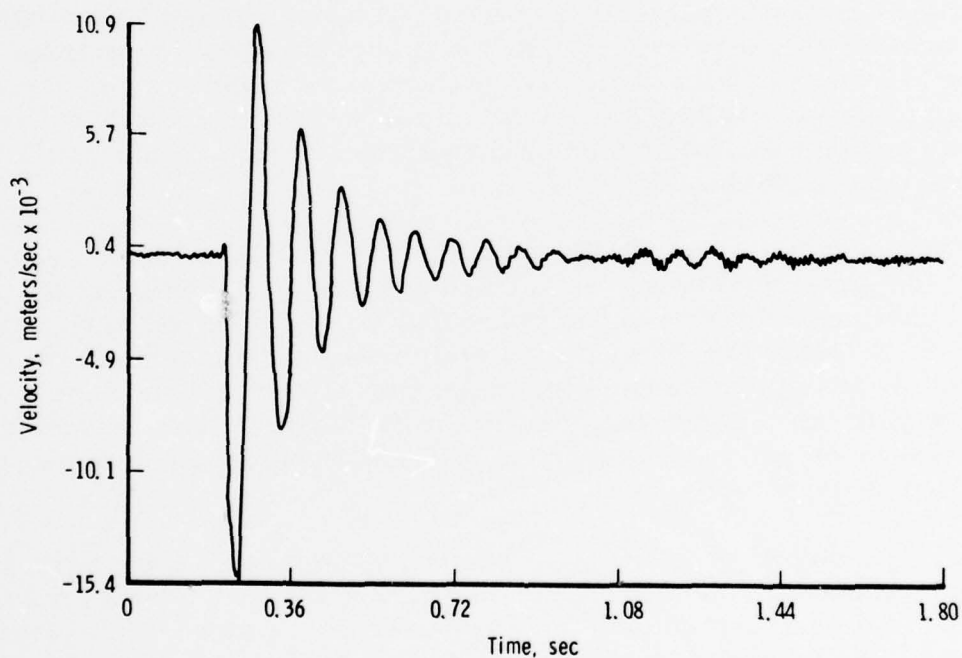
BASIC level programming was used to store each data array on magnetic tape for future reference and to convert the digital array from counts to meters and the analog array from volts to meters per second. Similar programming was used to integrate the analog velocity data and to scale and plot the data via an online graphics terminal thus providing the data curves given here.

For the data presented, 900 simultaneous analog (velocity) and digital (displacement) points were taken and plotted. A trapezoidal approximation of the area under every four points of the velocity data was used to obtain 225 integrated velocity (analog displacement) points. It should be noted that since fewer integrated velocity points were available for plotting, a somewhat coarser curve results. Also, some error should be expected in the integration process when high frequencies are contained in the velocity data.

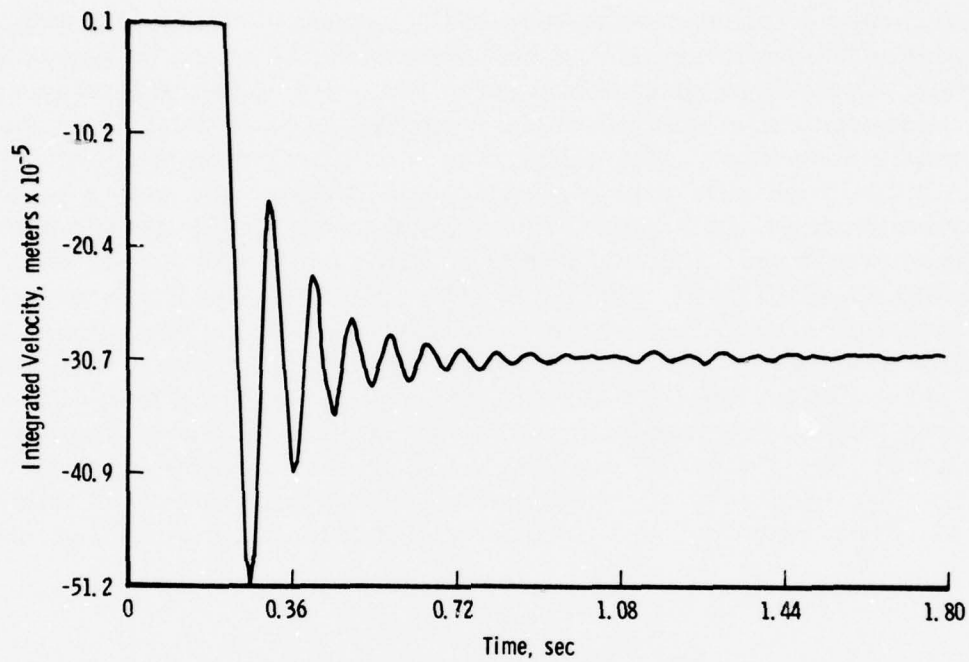
A large variety of bar oscillation runs were taken. Only three runs will be presented to show the dynamic range of the interferometer in addition to presenting the data from two different readout techniques: one from the digital processor (fringe counting), and the other from the analog processor (frequency-to-voltage conversion of the photodetector signal). The first two experiments that will be discussed use the primary optics module only, without beam expanding. The last run to be discussed used a beam-expanding module to produce 1-in. beams.

The first run is shown in Fig. 15. Both retroreflectors were mounted 7 in. apart on the oscillating bar, and initial displacement of

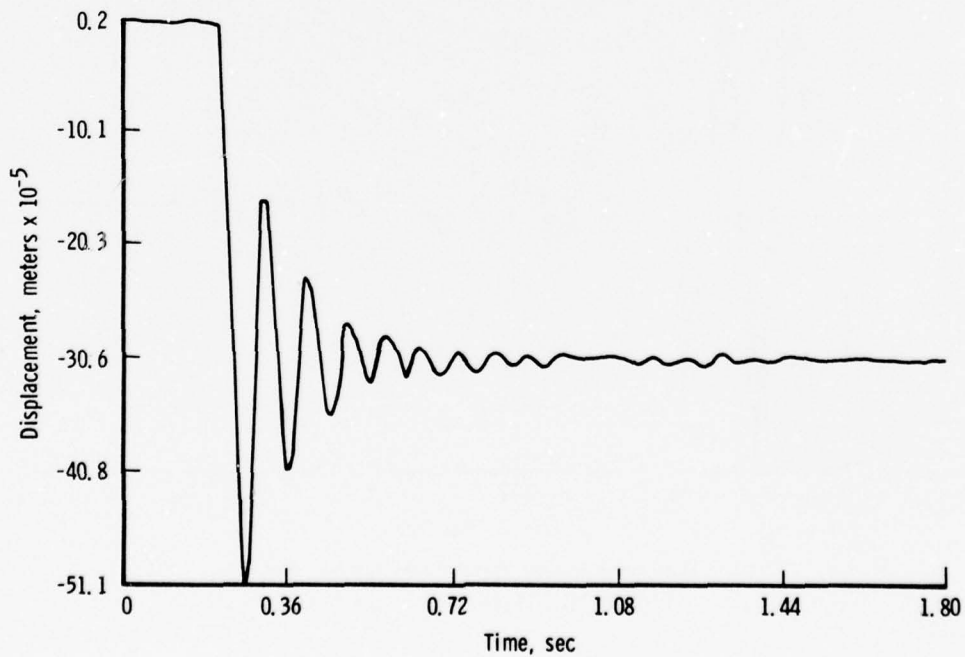
the bar was set at approximately 1.65 cm. The bar was strongly damped to reduce the fundamental and harmonic modes. Figure 15a displays the relative velocity between the two retroreflectors. This figure also shows some residual "background" vibrations of the bar from acoustic excitation. Computer integration yields Fig. 15b which is relative displacement between the two retroreflectors. The initial peak excursion is seen to be approximately 510μ with an immediate exponential decay to a final position of approximately 31μ . Direct fringe counting yields a displacement in steps of $\lambda/4$ or 0.16μ . Figure 15c is the plot of the fringe counting output (digital) which may now be compared to the integrated velocity data of Fig. 15b. Excellent agreement is seen between the two readout methods with almost identical peak amplitude excursions even though a "rough" integration technique is used in the analog method.



a. Online velocity data from analog readout
Figure 15. Data from Run No. 1.

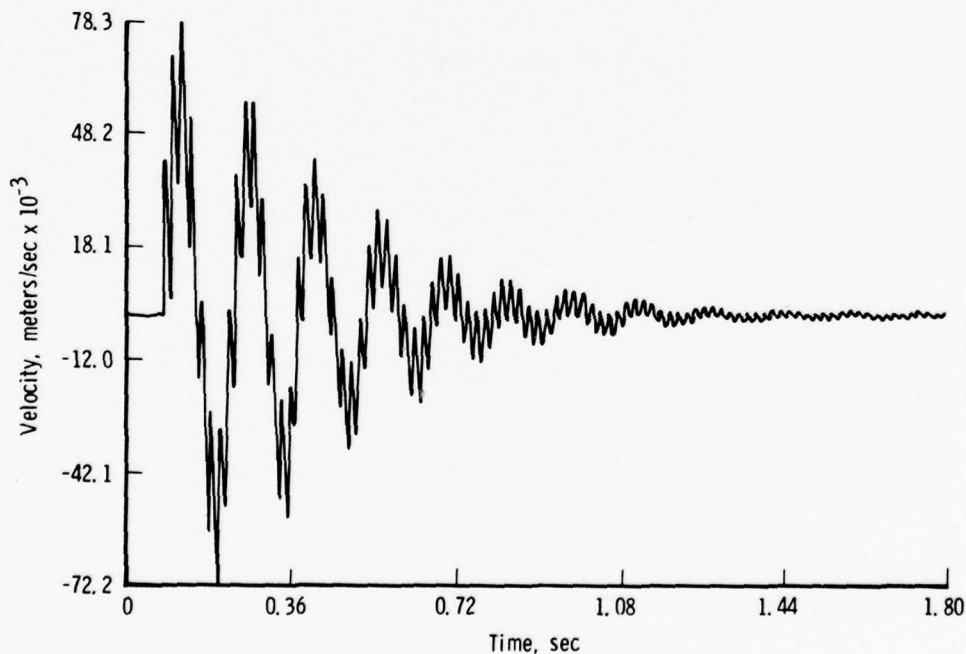


b. Integrated velocity of Fig. 15a

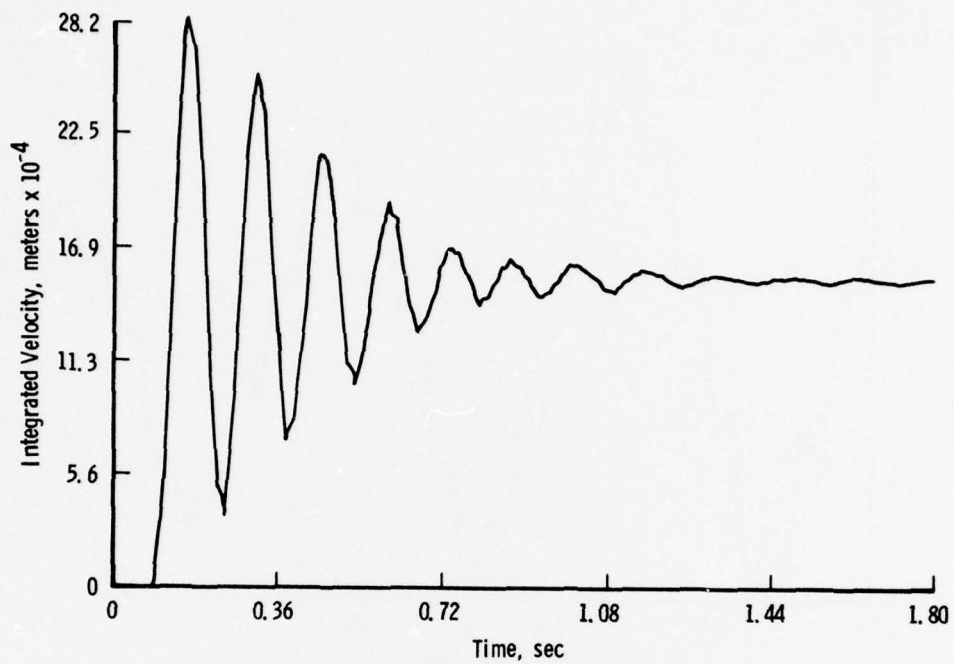


c. Online displacement data from digital readout
Figure 15. Concluded.

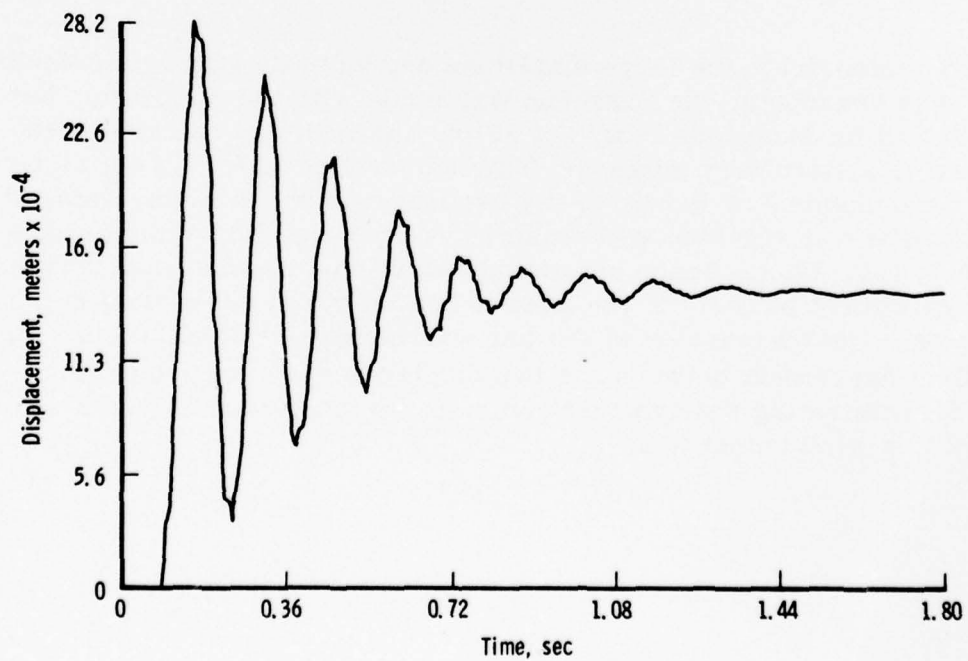
A larger displacement is seen in the second run (Fig. 16) with strong damping of the fundamental and moderate damping of the harmonic frequency. The same experimental setup was used as in the first run. The two frequencies are easily deduced from the velocity data, Fig. 16a, of the analog processor. The online computer integration is shown in Fig. 16b. Initial peak excursion is seen to be 0.282 cm with only a minor contribution from the higher frequency component. Figure 16c shows the displacement from the direct fringe counting processor and is seen to be virtually identical to the integrated velocity data. The fringe counting displacement also shows a peak amplitude of 0.282 cm identical to the integrated velocity. Since the fringe counting displacement data have a $0.16\text{-}\mu$ resolution, the data represented in the last 25 percent of the data run may be retrieved and analyzed. Figure 16d shows the last 25 percent of Fig. 16c easily showing the fundamental frequency with approximately $35\text{-}\mu$ amplitude and the harmonic at approximately $5\text{-}\mu$ amplitude thereby demonstrating the resolution available in large amplitude data.



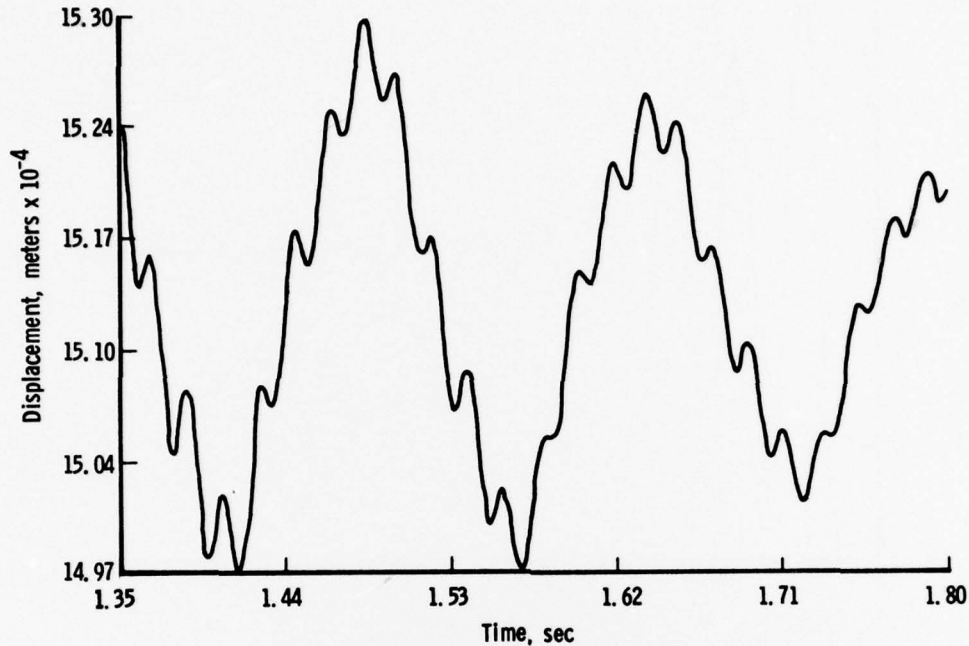
a. Online velocity data from analog readout
Figure 16. Data from Run No. 2.



b. Integrated velocity of Fig. 16a

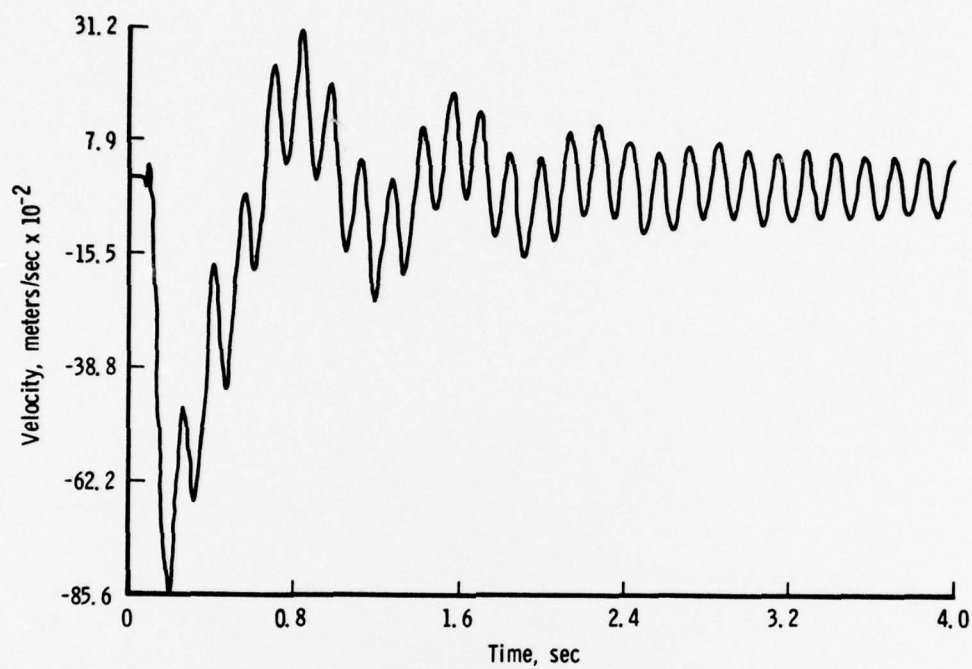


c. Online displacement from digital readout
Figure 16. Continued.

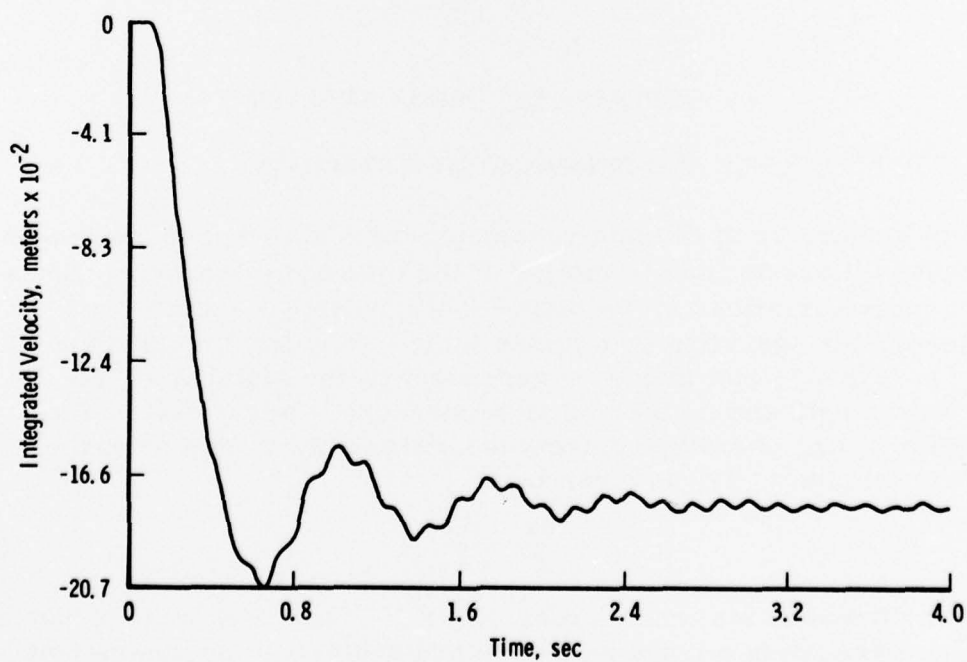


d. Instant recall of last 25 percent of Fig. 16c.
Figure 16. Concluded.

To demonstrate the large amplitude and velocity excursion capability of these readouts, the third run was made with the oscillating bar extended to its maximum length of 60 in. and with one retroreflector referenced to a stationary surface. This setup allowed for direct displacement measurement of the tip of the oscillating bar. A highly damped fundamental was obtained with minimal damping of the harmonic mode as shown in Fig. 17. A beam-expanding output module was incorporated in this experiment because of the lateral motion of the oscillating retroreflector. Peak excursion of the bar was measured to be 20 cm. Again, excellent agreement between the two displacement measurements is seen demonstrating the dynamic range of the interferometer and applicability to a wind tunnel test.

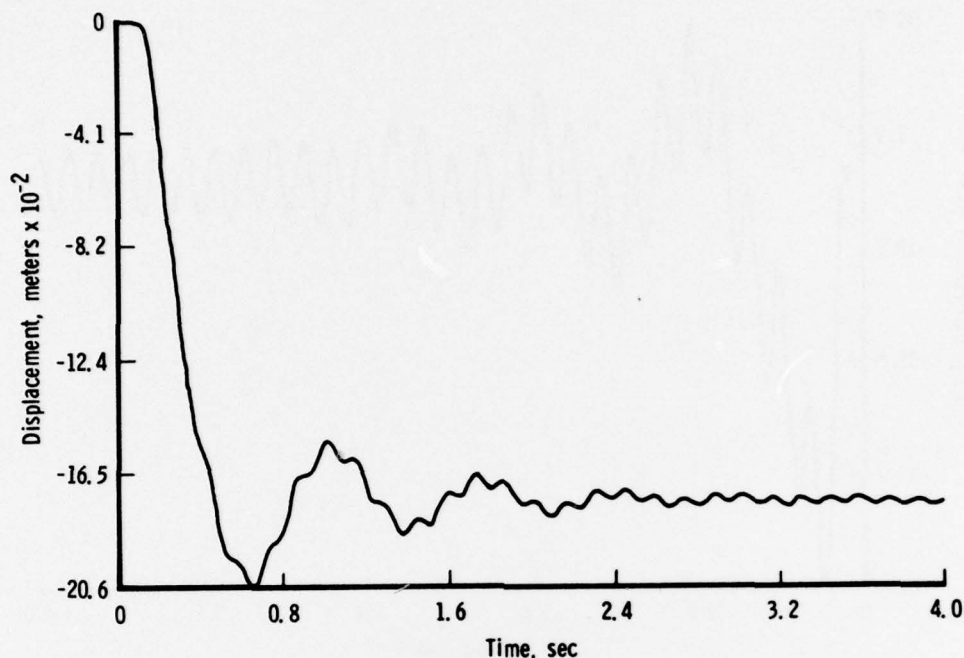


a. Online velocity data from analog readout



b. Integrated velocity of Fig. 17a

Figure 17. Data from Run No. 3.



c. Online displacement from digital readout
Figure 17. Concluded.

4.0 DISPLACEMENT ERROR ANALYSIS

4.1 LASER FREQUENCY AND OPTICAL SYSTEM STABILITY

The sensitivity of the interferometer for displacement measurements also makes it susceptible to motion of the optical system components and to frequency variations in the output of the laser. A laboratory interferometer operating on a stable table in a controlled environment has a theoretical accuracy dependent on the stability of the laser wavelength and on the ability to measure it accurately. The uncertainty, dx , of a displacement measurement, x , due to wavelength uncertainty, $d\lambda$, is given by

$$\frac{dx}{x} = \frac{d\lambda}{\lambda} \quad (37)$$

Wavelength stabilities on the order of $5 \times 10^{-7} \mu\text{m}$ over an 8-hr period using an intracavity air spaced etalon are achievable on commercially available lasers (Ref. 14). However, changes in the dimensions of the laser cavity and in the index of refraction of materials in the cavity due

to temperature changes and mechanical and acoustical vibrations will increase this value. The temperature stability of an etalon is $4 \times 10^{-8} \mu\text{m}/^\circ\text{C}$. Even with these variations the measurement accuracy of the interferometer is well within that required to measure model displacement in a wind tunnel.

A more important source of error in the displacement measurement is vibration of the optical components. A frequency shift induced in one of the heterodyned light beams caused by a relative displacement in one of the optical elements will introduce extraneous information into the displacement signal. Therefore, motion between optical elements must be kept to a minimum. This can be achieved with a compact, rigid, optical system mounted on a massive support isolated from acoustical and mechanical vibrations.

4.2 DENSITY EFFECTS

Since the interferometric technique measures the difference in length between two optical paths, the signal arising from the mixing of the two light beams is a function of not only the model position but the index of refraction along each of the two optical paths, L_1 and L_2 .

Applying Fermat's principle to Eq. (2) the relative variation of phase, $\Delta\phi$, between optical paths is

$$\Delta\phi = \phi_1 - \phi_2 = \frac{4\pi}{\lambda} \left[\int_{L_1} \eta_1(\ell, t) d\ell - \int_{L_2} \eta_2(\ell, t) d\ell \right] \quad (38)$$

where $\eta_1(\ell, t)$ and $\eta_2(\ell, t)$ are the time and spatially dependent indices of refraction along the optical paths L_1 and L_2 , respectively. Depending upon the complexity of η , and the geometry of the optical path, one can either solve this integral in closed form for simple cases or a solution may be obtained using numerical iterative techniques.

In an operating wind tunnel, density variations are quite evident. The greatest variance is the region between the tunnel wall and the free-stream region where the density is essentially constant. The transition region is called the boundary layer and varies as the tunnel operating conditions vary. The density effect or index of refraction variation upon the interferometric measurements must be considered. In air, the Lorentz-Lorentz relationship ($\eta \approx 1.0$) reduces to the Gladstone-Dale relationships given by

$$\eta - 1 = K\rho \quad (39)$$

where ρ is the air density and K is a proportionality constant. Assuming $\lambda = 0.6328 \mu$, then $K = 117 \times 10^{-3} \text{ ft}^3 \text{ slug}^{-1}$.

By far the largest effects will be due to variations in the tunnel from the time calibration measurements are made, through the transition to the particular tunnel operating conditions where the dynamic data are to be taken. Consider the operating envelope for the AEDC Propulsion Wind Tunnel Facility (PWT) 16T and 16S tunnels as shown in Fig. 18.

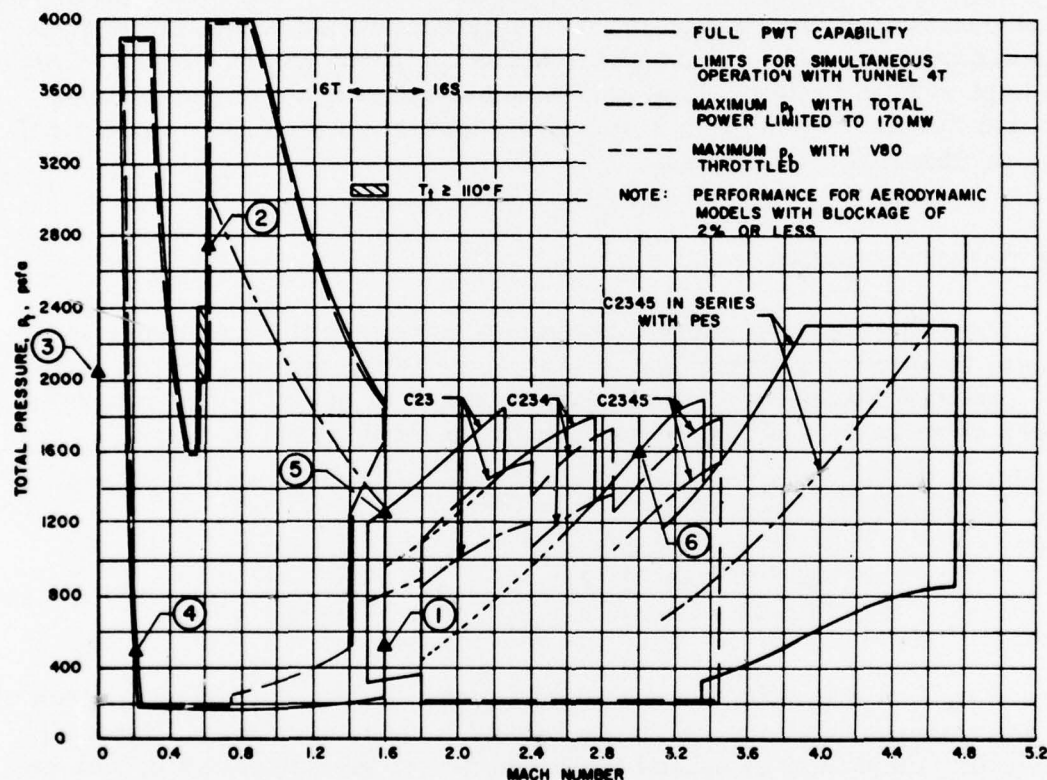


Figure 18. Total-pressure operating envelopes for PWT Tunnels 16T and 16S.

At the selected tunnel operating points the corresponding pressures and temperatures were used to calculate the free-stream density. Also, assuming the optical paths are in the direction of density gradients, such as boundary layers, Eq. (38) reduces to

$$\Delta\phi \approx \frac{4\pi}{\lambda} \Delta\ell \quad (40)$$

where $\Delta\ell$ is the change in optical pathlength due to either changes in η or in changes in L or both. The apparent phase change cannot be separated into index of refraction changes and changes in L without some

knowledge of the flow-field conditions. In general, this is easily obtained and even a simple first-order approximation will account for a large fraction of the variation in the optical path. As an example, the effects of the optical path in traversing to the center of a 16-ft test section under various tunnel conditions are illustrated. Given the typical data points in Table 2, the change in pathlength due to change in index of refraction from vacuum conditions can be calculated based on the total pressure, typical operating total temperatures, and Mach number. The air density in the tunnels can be calculated and consequently the index of refraction is obtained. Using the Gladstone-Dale equation, and Eq. (38), the maximum variation in optical path from vacuum conditions was calculated:

$$K\rho = \eta - 1 = \Delta\ell/\ell \quad (41)$$

Over an 8-ft distance, this can be as low as $49\ \mu\text{m}$ and as high as $687\ \mu\text{m}$ for extremes in the tunnel conditions as shown in Column 1 of Table 2.

Corrections for variations can be made in one of two ways: (1) by an on-the-body retroreflector to be used as a reference distance or (2) through calculations based on the knowledge of the tunnel conditions. The effects of boundary layers within the tunnel can also be included in the analysis. Semi-empirical relationships for the density through the boundary layer can be used in conjunction with the Gladstone-Dale equation to determine an effective index of refraction. An empirical relationship for the density variation through a boundary layer is given by

$$\frac{\rho}{\rho_\infty} = \frac{1}{1 + 0.2 M_\infty^2 \left(1 - \frac{y}{\delta_0}\right)^{2/9}} \quad (42)$$

where ρ = the density at position y from the chamber wall to the free-stream position δ_0 where the density is ρ_∞ . Assuming a boundary-layer thickness δ_0 of 1 ft and integrating through the entire boundary layer, an average ρ/ρ_∞ can be obtained for a given free-stream Mach number, M_∞ . As in the case of free-stream corrections, the variation over an 8-ft path was calculated. The maximum variation from free stream occurs for $M_\infty = 3.0$. This amounts to a 7.4-percent change in previously calculated optical path difference over 8 ft. By neglecting this correction, a maximum error of $13.7\ \mu\text{m}$ (87 counts in a $1/4\ \lambda$ system) would be incurred.

Table 2. Tunnels 16T/S Conditions

Data Point	Mach Number	P_o , psfa	P , psfa	T_o	T , °R	ρ_o , slug/ft ³	$\eta - 1$, $\Delta \ell / \ell$	①		②	
								Free Stream Only		Free Stream Plus Boundary Layer	Percent Difference from ①
								$\Delta \ell (\mu\pi)$, $\ell = 8$ ft	$\bar{\rho} / \rho_o$	$\Delta \ell (\mu\pi)$, $\ell = 8$ ft	
1	1.6	500	118	150°F 610°R	402	1.706×10^{-4}	1.997×10^{-5}	49	0.707	47.2	3.7
2	0.6	2,700	2,117	90°F 550°R	512	2.407×10^{-3}	2.816×10^{-4}	687	0.944	682	0.7
3	0	2,117	2,117	80°F 540°R	540	2.28×10^{-3}	2.675×10^{-4}	652	1.000	652	0
4	0.2	500	486	90°F 550°R	545	5.218×10^{-4}	6.105×10^{-5}	148	0.993	147.9	0.01
5	1.6	1,300	306	110°F 70°R	376	4.905×10^{-4}	5.538×10^{-5}	135	0.707	130.1	3.7
6	3.0	1,600	44	632°F 110°R	390	6.519×10^{-5}	7.62×10^{-6}	186	0.410	172.3	7.4

Density variations are evidenced in forms other than in the boundary layers. Under certain flow conditions in the transonic and supersonic operating region, shock waves are evidenced. Associated with the shock wave structure within a wind tunnel are strong density gradients. The effect of these gradients upon light beams passing through such a medium also changes the optical pathlength and introduces angular variations in the light path. In general, whenever the ray path is not in the same direction as the density gradient, then a refractive bending of the ray will occur. In the case of planar shock waves, the net result is a deviation in the original path for all plane parallel waves incident upon the shock front. With only a rudimentary knowledge of the flow conditions, the net change in optical path to a retroreflector located upon a model can be calculated with considerable accuracy.

The effects of conical shocks upon incident radiation is similar to wavefront distortion by a lens with aberrations. This effect becomes increasingly important with increasing cone angle and Mach number as the density variation across the shock becomes greater. Both the oblique traversing of the optical path in the shock system and the focusing effect of a conical shock can affect the integrated pathlength to a model surface.

A boundary layer, as a shock front, can also have refractive effects on light rays passing through it. The boundary layer, furthermore, can cause phase fluctuations which are of importance to interferometric technique. Fluctuating boundary layers can further cause image dancing, scintillation or loss in image resolution which are of particular importance in imaging systems design.

While it is beyond the scope of this report to comprehensively deal with each of the density related optical path deviations, it was shown that a major contributor, i. e., tunnel condition changes, while significant, can be calculated and used to reduce errors. Furthermore, the density effects can be reduced and in some cases, eliminated through the use of a reference beam taken from the model itself. This is due to the matching of optical path conditions accurately over the small spatial differences along each optical path. Under these conditions, density effects are minimized. In general, even when on-the-body reference beams are used, some knowledge of the flow field will be required to ensure accurate data analysis.

5.0 SUMMARY AND CONCLUSIONS

An interferometric technique has been proposed for measuring model displacement and deformation in a wind tunnel. A two-beam noncontact, point-measuring device with a resolution to one-quarter of the laser wavelength has been described. Data from this device may be recorded and reduced online and are computer compatible.

Relative measurements can be made of the model with the retroreflectors mounted on the wing and fuselage. An absolute measurement, for model position relative to a stationary reference, can be made by placing one retroreflector in a known atmosphere. Retroreflectors are used to maintain optical alignment throughout the span of model motion.

A polarization-sensitive optical system reduces interference effects of stray light from the model and optical surfaces and separates the path of the illumination beam from the return beam. The illumination is collimated to spotlight areas on the model containing a retroreflector to efficiently utilize the laser light. Diameter, position, and angle of the illumination beam are dictated by the amount and direction of reflector motion during the test. Optical-to-electrical signal conversion is performed by an avalanche photodiode which has wide bandwidth, high sensitivity, and low noise. Because of the efficiency of the photodiode, the laser source power can be relatively low, thereby minimizing, if not obviating, safety problems. The severe environment of a test cell requires that the optical system be compact and rugged and isolated from both acoustical and mechanical noise and vibration.

Displacement data can be recovered from the 15-MHz frequency-modulated carrier with either a phase quadrature digital pulse counting technique or a frequency-to-voltage conversion analog system. These data can be made available digitally for computer analysis and as an analog signal for immediate evaluation during and following a test.

The displacement interferometer is capable of resolving motion to $\lambda/4$ which for a helium-neon laser is 158.2 nanometers. Maximum surface velocity is limited by the bandwidth of the electronic signal processor. A maximum frequency deviation of 5 MHz from 15 MHz (10-MHz bandwidth) limits the velocity to 1.6 meters/sec. For oscillatory motion, the maximum peak amplitude-frequency product is 25.2 cm-Hz. Maximum displacement, on the other hand, is limited electronically by the number of up/down counters in the digital data processing circuit and by the maximum voltage and sensitivity of the analog system. With six and one-half digits in the readout of the phase quadrature digital system and $\lambda/4$ resolution, displacements of ± 31.64 cm can be measured.

Density gradients and other tunnel flow conditions can introduce variations in optical pathlength and introduce errors in the measurement. Techniques are available to compensate for these variations. Nevertheless, future work will include more detailed theoretical and experimental investigations into the refractive effects of shocks and boundary layers on the uniformity of the optical wavefronts at the photodetector. Vibration as well as acoustical effects on the optical package will be analyzed to determine the amount of isolation necessary to prevent the optical components from vibrating and introducing extraneous signals on the model displacement signal.

The two-beam system will be used in actual tunnel tests to analyze the effects of vibration and laser beam perturbations due to the tunnel flow conditions. A multiple-beam optical system will then be designed and built to increase the capability for simultaneous measurements of model attitude and deformation.

Electronic signal processors for the multibeam system will be fabricated with improvements incorporated in bandwidth and response as required for specific applications. The use of a microcomputer for the online acquisition and display of data from a set of multibeam readouts will be studied.

The possible replacement of the retroreflectors with highly reflecting tape or a diffuse surface will be analyzed. This would make model preparation much simpler. Means of reducing the number of optical components will also be studied. This includes scanning single or multiple laser beams across the surface and collecting the backscattered light by a single lens. Frequency multiplexing of the signals will be studied as a possible means of reducing the number of photodetectors in the multiple-beam system.

REFERENCES

1. Starr, R. F. and Schueler, C. J. "Experimental Studies of a Ludwig Tube High Reynolds Number Transonic Tunnel." Proceedings of the AIAA 11th Aerospace Science Meeting, Paper No. 73-212, Washington, D. C., January 1973.
2. Barker, L. M. "Laser Interferometry in Shock-Wave Research." Experimental Mechanics, Vol. 12, May 1972, pp. 209-215.

3. Kwaaitaal, Th. "Contribution to the Interferometric Measurement of Sub-Angstrom Vibrations." Review of Scientific Instruments, Vol. 45, No. 1, January 1974, pp. 39-41.
4. Deferrari, H. A., Darby, R. A., and Andrews, F. A. "Vibrational Displacement and Mode-Shape Measurement by a Laser Interferometer." The Journal of the Acoustical Society of America, Vol. 42, No. 5, 1967, pp. 983-990.
5. Eberhardt, F. J. and Andrews, F. A. "Laser Heterodyne System for Measurement and Analysis of Vibration." The Journal of the Acoustical Society of America, Vol. 48, No. 3 (Part 1), 1970, pp. 603-609.
6. Koronkevitch, V. P., et al. "Laser Interferometers and Measuring Displacements and Determining Object Positions." Applied Optics, Vol. 11, No. 2, February 1972, pp. 359-361.
7. Goethert, W. H. "Development and Application of a Laser Interferometer for Measurements of High Temperature Vibrating Surfaces." Masters' Thesis, University of Tennessee, March 1975.
8. The Opto-Electronics Data Book for Design Engineers, Texas Instruments, Inc., Dallas, Texas.
9. Delange, O. E. "Optical Heterodyne Detection." IEEE Spectrum, Vol. 5, October 1968, pp. 77-85.
10. Electro-Optics Handbook, RCA, Commercial Engineering, Harrison, N. J.
11. Born, M. and Wolf, E. Principles of Optics, Oxford, England, Pergamon Press, 1965.
12. Lay, C. M. "Interferometric Displacement Indication." Instruments and Control Systems, Vol. 43, May 1970, pp. 110-112.
13. Schwartz, M. Information Transmission, Modulation and Noise. McGraw-Hill Book Co., Inc. New York, 1970.
14. Data Sheet, Spectra-Physics Model 589 Air-Spaced Etalon, Spectra-Physics, Inc., Mountain View, Calif.

NOMENCLATURE

A	Zero-crossing detected signal of P_1
$V_m = 1, 2, \dots$	Electrical signal amplitude
$A(\theta_1)$	Effective aperture of retroreflector
B	Delayed A waveform
C	Zero-crossing detected signal of P_2
C_δ	Delayed C waveform
D	Down count pulse
D_o	Beam diameter leaving optics package
D_R	Diameter of retroreflector
d_L	Beam diameter prior to beam expanding optics
d_R	Diameter of returning beam inside optics package
d_1, d_2	Signal from 34-MHz and 49-MHz oscillator, respectively
E_o, E_R	Amplitude of object and reference beam
Δf	Bandwidth of electronics
f_1, f_2	Focal lengths
f_c	Carrier frequency (15 MHz)
$f(t)$	Signal frequency
$G_n = 1, 2, \dots$	Gain of electronic components
$g(t)$	Sum and difference electronic signal

H	Distance between output optics and model surface
I	Intensity incident on retroreflector
I_o, I_R	Intensity of object and reference beam
$i(t)$	Photodetector output
K	Proportionality constant
L	Lateral motion of model
L_1, L_2	Optical path length of object beam and reference beam
ℓ	Lateral motion
$M_1(t), M_2(t)$	Signal after mixing with reference oscillator signal
M_∞	Free-stream Mach number
N	Number of light beams generated
N_p	Noise term due to detector and optical noise
NEP	Noise equivalent power
n	Number of frequency division stages in analog processor
$P_1(t), P_2(t)$	Lowpass filtering of $M_1(t)$ and $M_2(t)$
R	Distance from point of rotation to retro-reflector
$r(t), r_1(t), r_2(t)$	Reference signals (see Fig. 7)
S	Retroreflector spacing
$S(t)$	Frequency-modulated signal

s	Beam spacing prior to beam-expanding optics
U	Up count pulse train
$\Delta v(t)$	Velocity difference between two retro-reflectors
x(t)	Reflector motion
y	Distance from chamber wall (inside of boundary layer)
α	Model rotation angle
β	Air-glass interface loss
γ	Retroreflector efficiency
δ	Polarization rotation angle upon reflection
δ_o	Boundary-layer thickness
ϵ	Bragg cell light deflection efficiency
η	Index of refraction
θ_i	Angle of incidence of light beam
θ_m	Maximum model illumination angle
λ	Optical wavelength
ρ	Density
$\phi_o(t), \phi_R(t)$	Phase term of object and reference beam
ω_c	Optical carrier frequency or $(\omega_o - \omega_R)$
ω_o	Angular frequency, object beam
ω_R	Angular frequency, reference beam
$\Delta\omega_\alpha$	Frequency deviation